Synthesis and Characterization of Wide Bandgap Absorber Layer for Stable Perovskite Solar Cells

Muneeza Ahmad

Reg # 00000204316

Session 2017-19

Supervised by

Prof. Dr. Nadia Shahzad

A Thesis Submitted to the U.S.-Pakistan Centre for Advanced Studies in Energy in partial fulfillment of the requirements for the degree of

MASTER of SCIENCE in

ENERGY SYSTEMS ENGINEERING

U.S.-Pakistan Centre for Advanced Studies in Energy

National University of Sciences and Technology (NUST)

H-12, Islamabad 44000, Pakistan

January 2021

<div align="center">**THESIS ACCEPTANCE CERTIFICATE**</div>

Certified that final copy of MS/MPhil thesis written by Ms. <u>Muneeza Ahmad</u> , (Registration No. <u>00000204316),</u> of <u>U.S.-Pakistan Center for Advanced Studies in Energy</u> has been vetted by undersigned, found complete in all respects as per NUST Statues/Regulations, is within the similarity indices limit and is accepted as partial fulfillment for the award of MS/MPhil degree. It is further certified that necessary amendments as pointed out by GEC members of the scholar have also been incorporated in the said thesis.

Signature: _____

Name of Supervisor _____ <u>Dr. Nadia Shahzad</u>

Date: _____

Signature (HoD): _____

Date: _____

Signature (Dean/Principal): _____

Date: _____

Certificate

This is to certify that work in this thesis has been carried out by **Ms. Muneeza Ahmad** and completed under my supervision in Solar Energy Laboratory, U.S-Pakistan Center for Advanced Studies in Energy, National University of Sciences and Technology, H-12, Islamabad, Pakistan.

Supervisor: _____

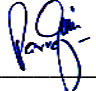   Dr. Nadia Shahzad
                                             USPCAS-E
                                             NUST, Islamabad

GEC member # 1:   _____

                                             Dr. Naseem Iqbal
                                             USPCAS-E
                                             NUST, Islamabad

GEC member # 2:   _____

                                             Dr.Parvez Akhter
                                             USPCAS-E
                                             NUST, Islamabad

GEC member # 3:   _____

                                             Dr. Afzal Kamboh
                                             PCRET
                                             Islamabad

HoD- (ESE)   _____

                                             Dr. Naseem Iqbal
                                             USPCAS-E
                                             NUST, Islamabad

Principal/ Dean   _____

                                             Dr. Adeel Waqas
                                             USPCAS-E
                                             NUST, Islamabad

Dedication

I dedicate this thesis and all the hard work that went into it to every girl or woman who has risen to the challenges in front of her and come out a winner.

Acknowledgement

I would like to thank my supervisor, Dr. Nadia Shahzad, for her constant support and guidance during my research work. I am also grateful to my GEC members Dr. Naseem Iqbal, Dr. Parvez Akhter and Dr. Afzal Hussain Kamboh for their valuable feedback and constructive criticism. Most of all I am indebted to my lab fellows and the lab engineers at USPCAS-E, for their help and assistance every step of the way.

Abstract

Wide bandgap perovskite solar cells are becoming the preferred choice for top cells in a tandem architecture with crystalline silicon solar cells. This is due to their bandgap tunability (1.6 to 3eV), low-temperature solution processing, fast charge carrier rate, long carrier diffusion length, and high absorbance in the visible region. Among the wide bandgap perovskites, a mixed cation, mixed halide composition containing $Cs_xFA_{1-x}PbI_{3-y}Br_y$ has is a popular choice because the presence of Br widens the bandgap and the addition of Cs stabilizes the crystal structure. However, these perovskite layers were fabricated using a one-step spin-coating technique even though sequential deposition promotes crystallization and offers bbetter film coverage. In this paper, we have fabricated a $Cs_{0.2}FA_{0.8}PbI_{3-x}Br_x$ perovskite absorber layer using sequential deposition. The concentration of Br was varied from 0 to 1, and the optical, structural and morphological properties of the film were studied. As the concentration of Br was increased, the perovskite showed better crystallinity however, beyond Br-0.3, the presence of another perovskite phase matching $CsPbBr_3$ was detected owing to a preference for the Pb-Br over the Pb-I complex. Optically, the perovskite films also skewed from the predicted bandgap for Br concentrations of 0.5 and 0.7. Their bandgap was in the 2 eV range, which also matches with $CsPbBr_3$. The morphology showed the presence of large grains with high surface roughness. This study explores compositional tuning via the sequential deposition route for a wide bandgap perovskite absorber layer.

Keywords: *perovskite, sequential deposition, wide bandgap, absorber, solar cell*

Table of Contents

List of Figures

List of Tables

List of Abbreviations

AEDB – Alternate Energy Development Board

CIGS – Copper Indium Gallium Selenide

DSSC – Dye-sensitized Solar Cell

FA – Formamidinium

MA – Methylammonium

PSC – Perovskite Solar Cell

UV-Vis – Ultraviolet Visible Spectroscopy

SEM – Scanning Electron Microscopy

XRD – X-ray Dispersive Spectroscopy

AFM – Atomic Force Microscopy

TPV – Themophotovoltaic

List of Publications

1. M Ahmad, N Shahzad, MA Tariq, A Sattar, "Investigating the Sequential Deposition Route for Mixed Cation Mixed Halide Wide Bandgap Perovskite Absorber Layer", *J. Electron. Mater.* (Under Review*)*

2. MA Tariq, N Shahzad, A Sattar, M Ahmad, M Anwar, M Shahzad, "Role of Bilayers to Realize Highly Efficient Stable Perovskite Solar Cells Based on CuSCN HTLs", *Renew. Sust. Energy Rev*. (Under Review)

Chapter 1: Background

1.1 Energy Crisis and Climate Change

The world's natural resources are in limited supply and depleting at an alarming rate. As the population keeps on increasing, the power consumption also increases. The natural resources are can take millenniums to replenish; so there is no other option but to conserve the resources we have and transition towards renewable energy resources [1]. Our country heavily relies on petroleum, natural gas and coal to harness energy. Around 80% of the world's oil resources have been tapped [2] and more than 50% of them have been consumed. If the rate of consumption remains the same, the world will run out of oil by the year 2040 [3].

Despite being a geographically and strategically important country, Pakistan has been suffering from an energy crisis from the 1980s. [4] Around 81% of the country's electricity is produced from oil and gas which has a total cost of 9.4 billion dollar. This accounts for 53% of our total imports and are a heavy burden on the economy. Climate change is another issue plaguing the nation. Although Pakistan's fossil fuel emissions are inconsequential in comparison to its neighboring developing countries [5], measures need to be taken to mitigate climate change. Pakistan is amongst the top 10 countries most vulnerable to climate change [5]. If fossil fuel consumption is not reduced, the country could spiral down this irreversible path.

1.2 Pakistan's Solar Potential

Pakistan has an abundant supply of sunshine. Because of its geographical location, the country receives sunshine throughout the year, averaging on 300 out of 365 sunny days [6]. Every day there is 8 to 10 hours of sunlight which equals to 15 MWh of solar radiation per year. This means Pakistan is capable of generation 1600 GW of solar power annually. In the 2015 solar assessment survey conducted by the World Bank, it was determined that Pakistan receives 2000 kWh/m^2 of AM 1.5 solar irradiation every year. Northern parts of Baluchistan receive the highest values which reach a maximum of 2700 kWh/m^2. Pakistan's weather is also ideal for solar energy generation because there are sizeable plains which are not affected by cloud coverage, aerosol content, irradiance diffusion or air pollution [7].

Another survey performed by the National Renewable Energy Laboratory in collaboration with many other organizations reveals that over 80% of the country is blessed with direct normal solar irradiation of 6 kWh/m^2/day [8]. Data provided by NASA when averaged out over 10-years also shows that solar insolation varies from 5-7 kWh/m^2/day.

1.3 Solar Energy Technologies

There are three major types of solar energy – solar photovoltaic (PV), solar thermal and concentrating solar power. Each of these converts sunlight into a form of energy that we can store for industrial, domestic and commercial use.

1.3.1 Solar Thermal

Solar thermal energy uses sunlight for heating and cooling purposes. The thermal energy is for water heating, space heating, and even cooling spaces [9]. The heat from solar radiation heats up the water which can be stored for later use or transferred to pipes for space heating. This technology can cut down on electricity and gas consumption in the winters.

1.3.2 Concentrating Solar Power

Concentrating solar power, or CSP for short, is mostly used for industrial purposes because of the large scale of the power plant [10]. The technology employs mirrors for reflecting the sunlight and directing it towards a receiver that collects it in the form of heat. This heat can later be used to produce electricity.

1.3.3 Solar PV

Solar Photovoltaic energy is the electricity created directly from sunlight using semiconductors. When solar radiation falls on a solar PV cell, the semiconductor frees electrons to generate an electric current [11]. Solar PV technology involves the use of solar cells which are connected in series and mounted on a module. Multiple modules can be arranged to form an array which makes up a solar panel. The number of arrays can be changed according to the amount of solar power required.

1.4 Working Principle of a Solar Cell

Solar cells rely on the photovoltaic effect which is the direct conversion of light into electricity. The most common type of solar cells uses two different semiconductor materials to form a junction and set up a potential difference [12]. A group III element impurity is added to one semiconducting material to create a valency making it the p-type (positive) material. The other is doped with a group V element with an extra electron creating an n-type (negative) material [13].

When the sunlight strikes the cell, the photons' energy is transferred to the electrons to create an electron-hole air. An electric field is created inside, and the charges separate. The electrons travel to the negative electrode while the holes rush towards the positive terminal. The load is

connected to both terminals in a series to drive an electrical current and provide power to any devices.
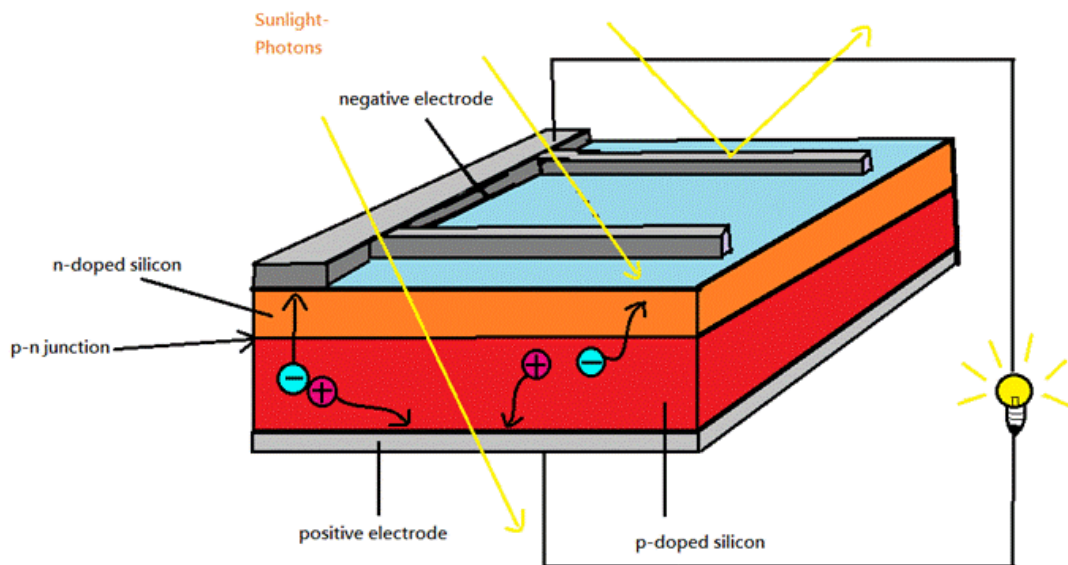
Figure 1: A diagram illustrating the mechanics behind a solar photovoltaic cell [13]

1.5 Current Status of Solar PV

Solar photovoltaic technology has been around in Pakistan since the 1980s. The government initially installed 18 systems with a total capacity of 450 kWh. However, these installations were largely unsuccessful because they did not produce the desired results. Lack of proper management and technical understanding led to the projects being abandoned [14]. Solar PV did not make a comeback until 2003 when the Alternate Energy Development Board (AEDB) was created. They took measures to promote renewable energy development and provide technical assistance [15]. AEDB offers financial benefits to investors to promote investment in the renewable energy market. At present, there are 28 solar power projects with a total capacity of 956.8 MW that are in the pipelines, NEPRA has awarded upfront tariffs on 472.48 MW to independent power producers and seven projects capable of generation 72.58 MW are in the financing stage.

1.6 Classification of Solar PV Cells

Solar cells are ordered into generations based on the materials used in them and the time period in which they were introduced [16]. There are four generations of solar cells.

1.6.1 First Generation

This includes mono and polycrystalline silicon solar cells. It uses wafer-based technology to create a light converting device. These solar cells are associated with high processing costs and wastage of material.

1.6.2 Second Generation

As a response to the limitations of the first generation, the second-generation solar cells reduced the film thickness and brought it down to the nanometer scale. They are called thin film solar cells and use materials such as amorphous silicon, cadmium indium gallium selenide (CIGS), cadmium telluride, and cadmium zinc tin sulfide (CZTS).

1.6.3 Third Generation

Light management using organic materials resulted in the third generation of solar cells. These include dye-sensitized solar cells, perovskite solar cells, photo chemical cells and quantum dot cells.

1.6.4 Fourth Generation

There has been a longstanding debate on whether there is a fourth generation of solar cells but generally the composites consisting of organic material with polymer matrix is included in this category.
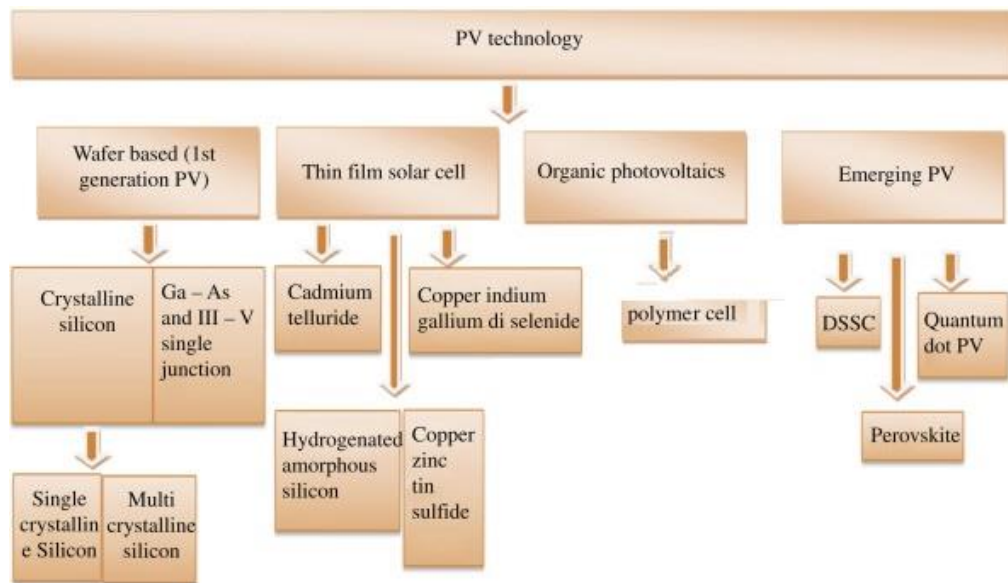
Figure 2: Classification of solar cells based on their generation [16]

1.7 Limitations of the Previous Generations

First generation includes silicon-based solar cells and even though they offer a high efficiency, silicon is not affordable. Moreover, the fabrication process is complex and there are high costs

associated with the materials [17]. There are also many loss mechanisms associated with the first generation: (i) the photons have energy greater than the cell bandgap so energy is lost and dissipated as heat and (ii) the Fermi level is lower of both p-type and n-type material is confined to the bandgap of silicon so the open-circuit voltage is minimized [18].

The basis of the second generation is thin film technology and it is lower in cost to the first generation and the cells have a higher absorption coefficient [19]. However, their fabrication processes are susceptible to environmental contamination and the materials are not easily accessible. The third generation of solar cells addresses these issues with readily available materials, a greater theoretical efficiency limit, and simple fabrication techniques.

1.8 Opportunities in Perovskite Solar Cells

Perovskite solar cells are the solution to the high costs associated with the previous cells and when used in tandem with another solar cell, they can cross the theoretical efficiency limit [20]. The wide bandgap perovskite solar cells are the most popular choice for multi-junction tandem architectures. However, they suffer from their own problems associated with the quality of the film which affects the stability of the entire cell structure [21]. The quality is inherently related to the deposition method which has primarily been one-step deposition through spin coating. It has been shown in the literature the two-step deposition process offers better control over the quality of the film since the method is broken down into two parts [22]. This is the challenge we will address in our research.

1.9 Objectives of the Research

- Synthesis of formamidinium iodide using rotary evaporator.
- Selection of a suitable chemical composition for a wide bandgap perovskite solar cell that is stable under light irradiation
- Synthesis of the absorber layer for a wide bandgap perovskite solar cell using sequential deposition
- Characterize the morphological, optical and electrical properties of the film

Table 1: Classification of Solar Cells

Type of Solar Cell								
Cell Generation	Mono-Si	Poly-Si	Amorphous Si	CdTe	CIGS	Perovskites	DSSC	Organic
Highest Efficiency	26.7%	23.2%	10.2%	21.0%	23.35%	24.2%	11.9%	13.45%
Area (cm^2)	79.0	3.923	1.001	1.0623	1.043	0.0955	1.005	0.04137
Costs ($/W)	1.2	1.2	0.75	0.5	0.75	0.25	<0.5	1.0
Advantages	Si easily available	Lower costs	Higher absorption and bandgap	Ideal bandgap, good stability	Slow degradation	Low-cost manufacturing and high efficiency	Environment friendly	Flexible design
Disadvantages	Expensive processes	Lower efficiency	Fast degradation	Cd is toxic	Sensitive to module defects	Low stability	Low efficiency	Low V_{OC}
References	[23]	[24]	[25]	[26]	[27]	[28]	[29]	[30]

Summary

The world is headed towards an energy crisis and will completely exhaust all oil reserves by 2040. Pakistan too, relies on natural oil for 81% of the electricity production and is one of the top ten countries most susceptible to the threat of climate change. Thankfully, our country receives an abundance of sunlight with 80% of the land getting direct solar insolation of 6 $kWh/m^2/day$. These favorable conditions indicate the country can benefit from the full range of solar technologies i.e., solar photovoltaic, concentrated solar power and solar thermal energy. Solar photovoltaic utilizes the energy of sunlight to create an electronic and hole current which can be used to power a load. AEDB is promoting the adoption of solar PV by offering financial benefits and currently there are 28 solar projects across Pakistan at various stages of completion which together can generate 956.8 MW. There are mainly three generations of solar photovoltaic cells. The first generation used Silicon, but the fabrication technology was too expensive. Second generation utilize thin film technology, but their production is also susceptible to contamination. The third generation uses organic materials and is free of the issues faced by its previous generations. Perovskite solar cells offer many advantages over the previous generations, the biggest of which is that in tandem they can cross the theoretical efficiency limit. Their deposition method however affects their film quality and switching to a two-step deposition could allow the means to control the absorber layer. The objective of this research is to select a suitable composition for the wide bandgap absorber layer for perovskite solar cells. The objectives also include fabrication and characterization of the above-mentioned layer.

References

[1]   "Causes and Solutions to the Global Energy Crisis - Conserve Energy Future." [Online]. Available: https://www.conserve-energy-future.com/causes-and-solutions-to-the-global-energy-crisis.php. [Accessed: 29-Nov-2019].

[2]   G. T. (George T. Miller and S. Spoolman, *Living in the environment*. .

[3]   "It's About Forty Years Until the Oil Runs Out | Stanford Graduate School of Business." [Online]. Available: https://www.gsb.stanford.edu/insights/its-about-forty-years-until-oil-runs-out. [Accessed: 29-Nov-2019].

[4]   "Energy crisis in Pakistan." [Online]. Available: https://nation.com.pk/21-Jun-2019/energy-crisis-in-pakistan. [Accessed: 29-Nov-2019].

[5]   Y. Wang, S. A. A. Shah, and P. Zhou, "City-level environmental performance in China," *Energy, Ecol. Environ.*, vol. 3, no. 3, pp. 149–161, Jun. 2018.

[6]   M. Wakeel, B. Chen, and S. Jahangir, "Overview of Energy Portfolio in Pakistan," 2016.

[7]   S. Stökler, C. Schillings, and B. Kraas, "Solar resource assessment study for Pakistan," *Renewable and Sustainable Energy Reviews*, vol. 58. Elsevier Ltd, pp. 1184–1188, 01-May-2016.

[8]   National Renewable Energy Laboratory, "Office of Energy Efficiency and Renewable Energy - Strategic Plan," 2016.

[9]   "Solar Heating & Cooling | SEIA." [Online]. Available: https://www.seia.org/initiatives/solar-heating-cooling. [Accessed: 29-Nov-2019].

[10]   "Solar Energy Technology Basics | Department of Energy." [Online]. Available: https://www.energy.gov/eere/solar/articles/solar-energy-technology-basics. [Accessed: 29-Nov-2019].

[11]   "Solar PV | Student Energy." [Online]. Available: https://www.studentenergy.org/topics/solar-pv. [Accessed: 29-Nov-2019].

[12]   "Molecular Expressions Microscopy Primer: Physics of Light and Color - Solar Cell Operation: Interactive Tutorial." [Online]. Available: https://micro.magnet.fsu.edu/primer/java/solarcell/. [Accessed: 29-Nov-2019].

[13]   "PVinsights: Solar PV Principle." [Online]. Available: http://pvinsights.com/Knowledge/Principle.php. [Accessed: 29-Nov-2019].

[14]   L. Xu, Y. Wang, Y. Solangi, H. Zameer, and S. Shah, "Off-Grid Solar PV Power Generation System in Sindh, Pakistan: A Techno-Economic Feasibility Analysis," *Processes*, vol. 7, no. 5, p. 308, May 2019.

[15]   "AEDB - Pakistan." [Online]. Available: http://www.aedb.org/. [Accessed: 29-Nov-2019].

[16]   "Solar Cell - an overview | ScienceDirect Topics." [Online]. Available: https://www.sciencedirect.com/topics/materials-science/solar-cell. [Accessed: 29-Nov-2019].

[17]   M. T. Kibria, A. Ahammed, M. Saad, F. Sony, and S.-U.-I. Hossain, "A Review: Comparative studies on different generation solar cells technology."

[18]   "An Introduction to Solar Cell Technology." [Online]. Available: https://cnx.org/contents/3QU3ovtd@1/An-Introduction-to-Solar-Cell-Technology. [Accessed: 29-Nov-2019].

[19]   "Solar energy as Renewable and alternative energy, Solar technology & energy information." [Online]. Available: http://www.altenergy.org/renewables/solar.html. [Accessed: 29-Nov-2019].

[20]   A. De Vos, "Detailed balance limit of the efficiency of tandem solar cells," *J. Phys. D. Appl. Phys.*, vol. 13, no. 5, pp. 839–846, 1980.

[21]   M. Saliba, J.-P. Correa-Baena, M. Grätzel, A. Hagfeldt, and A. Abate, "Perovskite Solar Cells: From the Atomic Level to Film Quality and Device Performance," *Angew. Chemie Int. Ed.*, vol. 57, no. 10, pp. 2554–2569, Mar. 2018.

[22]   Y. Wu, X. Yang, C. Qin, J. Liu, K. Zhang, and L. Han, "Retarding the crystallization of PbI 2 for highly reproducible planar- structured perovskite solar cells via sequential deposition," pp. 1–5, 2014.

[23]   K. Yoshikawa *et al.*, "Silicon heterojunction solar cell with interdigitated back contacts for a photoconversion efficiency over 26%," *Nat. Energy*, vol. 2, no. 5, pp. 1–8, Mar. 2017.

[24]   "Solar Panel Company & Solar Energy Information | Trina Solar." [Online]. Available: https://www.trinasolar.com/us/our-company. [Accessed: 05-Sep-2020].

[25]   H. Sai, T. Matsui, H. Kumagai, and K. Matsubara, "Thin-film microcrystalline silicon solar cells: 11.9% efficiency and beyond," *Appl. Phys. Express*, vol. 11, no. 2, p. 022301, Feb. 2018.

[26]   F. Solar, "First solar builds the highest efficiency thin film PV cell on record," *First Sol.*, vol. 5, 2014.

[27]   M. Nakamura, K. Yamaguchi, Y. Kimoto, Y. Yasaki, T. Kato, and H. Sugimoto, "Cd-Free Cu(In,Ga)(Se,S)2 thin-film solar cell with record efficiency of 23.35%," *IEEE J. Photovoltaics*, vol. 9, no. 6, pp. 1863–1867, Nov. 2019.

[28] "Insight in Science > UST ON (Webzine) > UST Story > University of Science & Technology." [Online]. Available: https://www.ust.ac.kr/cop/bbs/BBSMSTR_000000000552/selectBoardArticle.do?nttId =52667. [Accessed: 05-Sep-2020].

[29] R. Komiya, A. Fukui, N. Murofushi, N. Koide, R. Yamanaka, and H. Katayama, "Improvement of the conversion efficiency of a monolithic type dye-sensitized solar cell module," in *Technical Digest, 21st International Photovoltaic Science and Engineering Conference*, 2011, vol. 2.

[30] "University of Potsdam." [Online]. Available: https://www.uni-potsdam.de/en/university-of-potsdam.html. [Accessed: 05-Sep-2020].

Chapter 2: Potential for Perovskite Solar Cells

Perovskites are named after the naturally occurring mineral because it also has an orthorhombic crystal structure. The chemical formula for perovskites is denoted by ABX_3 where

- A = monovalent cation (Methylammonium, Cesium, Formamidinium, etc.)
- B = divalent metal cation (Pb, Sn, Ge, etc.)
- X = halide anion (I, Cl, Br, etc.) [1]
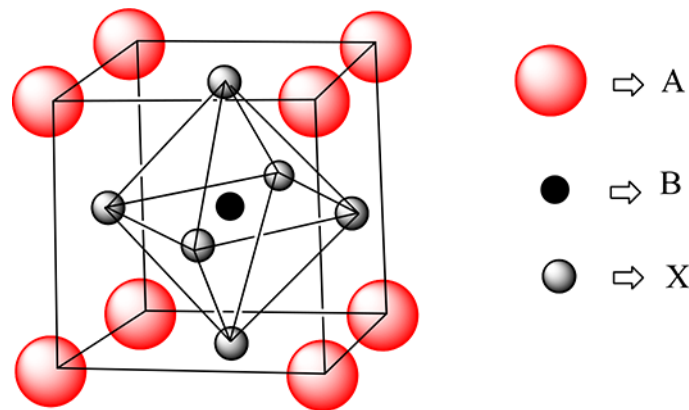
Figure 3: Perovskite Crystal Structure [2]

The compositions can be varied and intermixed to fabricate a perovskite crystal structure as long as the atomic size variances are within the tolerance factor [3]. This property can be used to tune the bandgap of the perovskite material over a wide range; from 1.15 to 3 eV i.e. infrared to ultraviolet [4]. Perovskites also possess other attractive properties such as high absorbance over the visible spectrum range, resistance to defect formation, fast carrier transport and long hole/electron diffusion length [5]. Furthermore, the solutions are processed at low temperatures, the materials are abundantly available and the material can be chemically tuned which make it a viable option for large-scale production of low cost and flexible solar cells [6].

The technology has gone through rapid breakthroughs and the power conversion efficiency has increased to over 25% in the last decade. The rapid success has made organic-inorganic lead halides a contender for the commercialized crystalline silicon, thin film and CdTe photovoltaic cells [7]. Single-junction perovskite solar cells follow two architectures the standard n-i-p and the inverted p-i-n structure. For the n-i-p solar cells the electron transport layer (ETL) is on a glass substrate coated with a transparent conductive coating, the hole transport later (HTL) is on the top with the absorber layer sandwiched in the middle. In the p-i-n, the order is reversed.
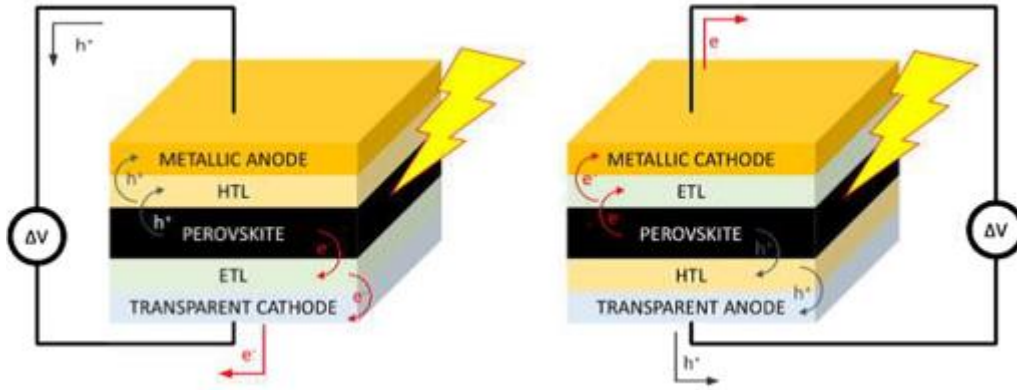
Figure 4: n-i-p (left) and p-i-n perovskite solar cell architecture [8]

2.1 Types of Perovskite Solar Cells

Single-junction perovskite solar cells can be classified into two categories based on the absorber layer bandgap. Wide bandgap cells are those with $E_g > 1.55$ eV and low bandgap are the ones with $E_g < 1.55$ eV. Wide bandgap perovskites are used as a top cell in tandem architectures and this is the reason why they are fabricated with a transparent back contact. Whereas low bandgap perovskites can be used as the bottom cell in perovskite-perovskite tandem solar cells.

2.1.1 Wide Bandgap PSCs

Wide bandgap PSCs with E_g between the ranges of 1.7 to 1.9 eV are used in tandem with crystalline silicon and low bandgap thin film PSCs. The bandgap can be achieved by substituting the iodide anion with bromide. Increasing the Br⁻ content can result in a wider bandgap for the perovskites. The figure below shows one example of how increasing the Br- anion concentration can increase the bandgap of MA-Pb halide perovskite.
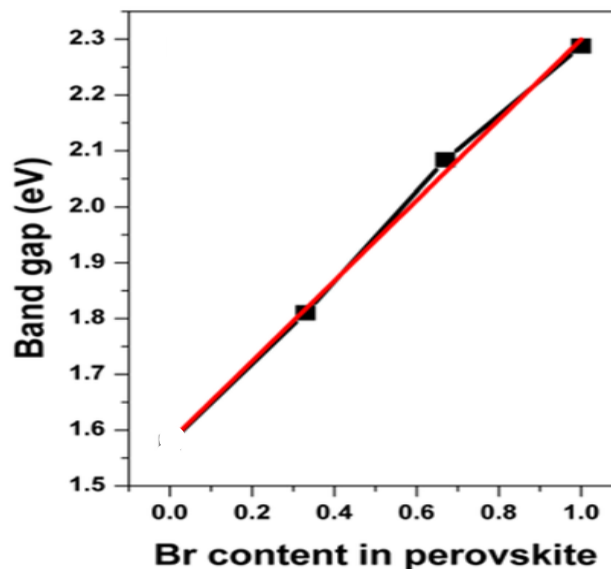
Figure 5: The effect of Br- concentration on the bandgap of MAPb(I$_{1-x}$Br$_x$)$_3$ [9]

25

2.1.2 Low Bandgap PSCs

Low bandgap PSCs include the standard methylammonium lead iodide with a 1.55 eV bandgap. Those with an even lower bandgap operate in the infrared region with a bandgap of 1.2 to 1.4 eV. Partially substituting the b with Sn can help achieve the lower E_g [10] and provide high conductivity as well [11]. However, the device durability is shorter and stability much poorer than the perovskites with a wider bandgap. The graph below depicts the change in bandgap as a result of the substitution of the metal ion Pb with the less toxic Sn in a methylammonium-based perovskite material.
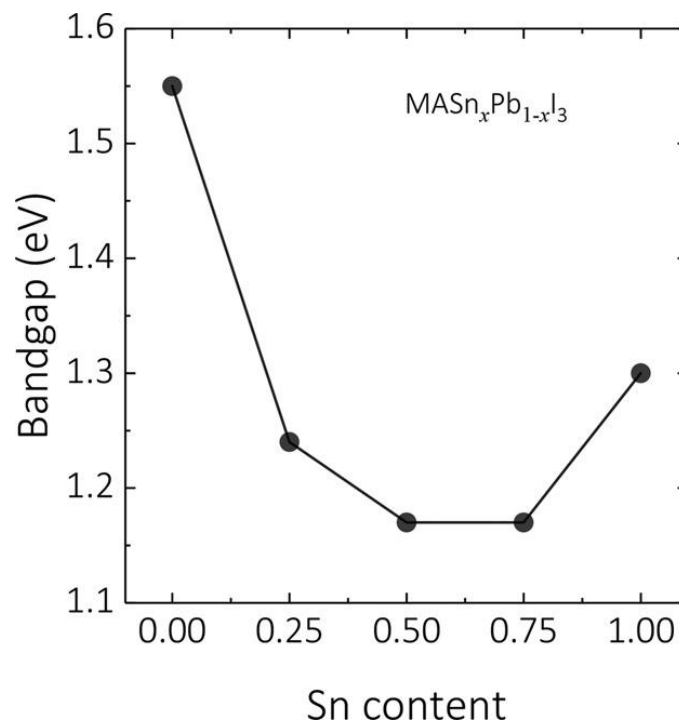
Figure 6: The change in bandgap as Pb is slowly replaced by Sn [12]

2.2 Challenges faced by Perovskite Solar Cells

Perovskite solar cells have not yet been commercialized due to some major performance setbacks. These challenges are related to the stability, lifetime and output of the devices.

The biggest issue faced by methylammonium (MA) cations is the degradation of the perovskite and degrading into the yellow phase. This affects the stability of the material and makes it especially sensitive to a rise in temperature. The MA containing perovskite solar cells can start deteriorating when brought into contact with moisture or heat starting from 85°C [13].

Defects are the major cause for poor performance of the device. The defects develop during the deposition which controls the quality, coverage and roughness of the film [14]. Intrinsic defects which are accumulated at interfaces can lead to low mobilities. This is the cause behind hysteresis often observed in the I-V curves [15]–[17].

Another issue introduced by defects is recombination loss. All charge carriers are not collected because some of them are lost due to the recombining of electrons and holes before they reach the electrode. Surface defects, interface defects and bulk defects introduce regions where the recombination occurs and leads to a nonradiative open-circuit voltage loss [18].

Efficiencies for low bandgap PSCs are well below the Shockley Queisser limit because there is a shortfall in the potential as the Sn^{2+} is oxidized to Sn^{4+}. For wide bandgap perovskites, the mixing of iodide and bromide ions can cause phase segregation and reverse the formation of perovskite phase [19], [20] leading to undesirable recombination centers.

2.3 Deposition Methods for PSCs

The selection of an appropriate fabrication method for the perovskite absorber layer is important because it affects the film thickness, crystallinity, morphology and purity. All these factors affect the performance of a solar cell [21]. There are many deposition methods being used for perovskite films, but the most common ones are one-step spin coating, two-step solution processing, vapor deposition and vapor-assisted solution process methods.

2.3.1 One-Step Spin Coating
The one-step synthesis route utilizes a solution processing technique wherein the lead halide and organic salts are dissolved in a solvent to create one precursor solution. The solvents are used in a stoichiometric ratio to tune the composition of the perovskite film. This solution is then spin coated directly on to the substrate coated with the charge transport layer after which it is dried to form the light-absorbing layer [22]–[24].

2.3.2 Two-Step Sequential Deposition
A two-step solution processing deposition technique involves two different precursor solutions which are sequentially deposited on to the substrate [25], [26]. The first step involves a lead halide dissolved in an appropriate solvent and then spin coated onto the charge transport layer. The coated substrate is dipped into a solution containing the cation salts and rinsed with the solvent to create a perovskite layer. The lead halide film reacts with the salts in which it is immersed to achieve successful synthesis.

2.3.3 Vapor Deposition
The vapor deposition is another method that can be used to deposit the absorber layer and it is performed under high vacuum. The lead halides and organic salts are either deposited alternately or simultaneously on the substrate. The technique utilizes thermal evaporation with dual sources to form a perovskite layer [27]–[29]. High temperatures and suitable atmospheric conditions are required for this process.

2.3.4 Vapor Assisted Solution Process

Vapor-assisted solution processing is a low-cost method for fabricating high quality light-harvesting perovskite films. It overcomes the issues associated with the standard solution or vapor processed methods. The lead halide solution is deposited on to a glass substrate using a solution processing technique. The organic salt is vaporized at temperatures of 120-165°C in an inert environment and the perovskite film grows on the substrate in a few hours [30]–[32].

2.4 The Deposition Effect

The film quality and inherent properties of the perovskite layer are reliant on the synthesis and fabrication process. The most common method for depositing an absorber layer is one-step spin coating because it is a simple, low-cost method. However, the morphology and crystallite size are not easy to control. The choice of solvents with a high solubility constant for both salts is also limited [33].

The sequential deposition technique offers a better cell performance as compared to the one-step method. The sequential process allows more control of the crystallization process because the perovskite is divided into two precursor solutions [34]. The two step-method is more suitable for environments where the humidity is higher as long as it is not above 60% [35]. The only problem with sequential deposition is that there is little control over the film thickness as compared to with vapor processing techniques.

Vapor deposition is one way to achieve highly uniform films with fewer pinholes and defects however, very high temperatures are required to vaporize PbI_2 salt [27]. The thermal evaporation equipment is highly specialized and releases toxic gases into the environment. The search for a non-toxic metal halide with a low evaporation temperature is ongoing.

With the vapor-assisted solution process, it is difficult for the lead halide film to completely react with the organic salt vapor which increases the internal resistance of the solar cell. Even though the process combines the best of both solution and vapor-based techniques, it comes at a price [36].

Table 2: Solar cells fabricated using different deposition methods

Year	Methodology	Results	Materials	Reference
2018	One step spin-coating	Maximum PCE of 17.8% with 83% recovered performance after 60 days in ambient air	**ETL:** PCBM **Absorber:** MAPbI$_3$ **HTL:** PEDOT:PSS	[37]
2012	One step spin-coating	Jsc of 16.1 mA/cm^2, Voc 0.631 V corresponding to a PCE of 5.5%	**ETL:** TiO$_2$ nanosheets **Absorber:** MAPbI$_3$ **HTL:** None	[38]
2013	Sequential deposition	A high Jsc of 20 mA/cm^2 and Voc of 993 mV with a PCE reaching 15%	**ETL:** TiO$_2$ **Absorber:** MAPbI$_3$ **HTL:** Spiro-MeOTAD	[39]
2014	Sequential deposition	The Jsc increased to 17.7 mA/cm^2 Stabilized PCE of 10.2%	**ETL:** TiO$_2$ **Absorber:** MAPbI$_3$ **HTL:** Spiro-MeOTAD	[40]
2013	Vapor deposition	15.4% efficiency with a Jsc of 21.2 mA/cm2 and Voc of 1.05V	**ETL:** TiO$_2$ **Absorber:** MAPbI$_3$ **HTL:** Spiro-MeOTAD	[41]
2017	Vapor deposition	Average V$_{OC}$ of 1.05V with a 17.3% PCE	**ETL:** C60 **Absorber:** MAPbI$_3$ **HTL:** TaTm	[42]
2014	Vapor-assisted solution process	Voc of 924 mV with an efficiency of 12.1%	**ETL:** TiO$_2$ **Absorber:** MAPbI$_3$ **HTL:** Spiro-MeOTAD	[43]
2015	Vapor-assisted solution process	Highest efficiency of 12.1%	**ETL:** TiO$_2$ **Absorber:** MAPbI$_3$	[44]

2.5 Deposition Routes Used for Wide Bandgap PSCs

Wide bandgap PSCs with E$_g$ over 1.7 eV is ideal for the top sub cell in tandem with both crystalline silicon and low bandgap PSC bottom sub cells [45]. The bandgap can be achieved by substituting the iodide anion with bromide. Increasing the Br- content can result in a wider bandgap for the perovskites [46]. The Cs-FA, mixed cation wide bandgap perovskite, is also more thermally stable than MAPbI$_3$ [47]. Many researchers have realized the importance of wide bandgap perovskites and dedicated their resources to improve efficiency and stability. McMeekin et al. substituted the formamidinium cation with cesium to eliminate phase instability of the halide domains and achieve a wide bandgap for tandem solar cell applications

[48]. The addition of Cs also widens the bandgap, and they exploited that property to push the Br-to-I unstable phase to a higher energy space. For a large part of the range, the bandgap for the $FA_{0.83}Cs_{0.17}Pb(I_xBr_{1-x})_3$ perovskite was predictable and followed Vegard's law. The absorber layer displayed long electron/hole diffusion length, high carrier mobility, and a large recombination resistance. The champion cell exhibited a short current density equal to 19.4 mA cm^{-2} with an open-circuit voltage of 1.2 V, and a PCE of 17.1%, which opens possibilities for a tandem cell to have over 30% efficiency.

Lin et al. verified that solution-processed hybrid perovskite solar cells provide great opportunities in tandem architecture because they eliminate the need for lattice matching and require low-temperature deposition methods [49]. They added Cs to the FA-based perovskites because it brings stability to the perovskite film under illumination.

The wide bandgap perovskite films are, however, sensitive to moisture, light, and temperature. Szostak et al. monitored the effects of relative humidity on a $Cs_yF_{1-y}Pb(I_xBr_{1-x})_3$ perovskite thin film. The choice of material was due to its bandgap tunability and because it is has been successfully applied in tandem with silicon solar cells [50]. They used a two-step spin coating procedure inside a nitrogen-filled glove box. The relative humidity level was maintained at 3-5%, 20%, and 40%. As the humidity level increased the power control efficiency of the cells decreased due to the growth of undesirable phases and non-uniform morphology of the film.

Zhou et al. addressed the phase segregation under illumination of a wide bandgap perovskite absorber layer by using additives in the precursor solution [51]. The addition of Cs to the mix improves stability under light due to the reduction in lattice size, increased entropy, and quenching of electron-phonon coupling. The absorber film's grain size and crystallinity were further enhanced by using excess FAI/FABr and PbSCN. The additives healed grain boundaries, improved the grain size and aided the crystallization of the absorber layer. They achieved a high output efficiency of 17.1% with a stable V_{OC} of 1.24 eV.

Zhou et al. improved the thermal and photostability of the wide bandgap absorber layer by utilizing a benzylamine post-treatment on the film [52]. The $FA_{0.85}Cs_{0.15}Pb(I_{0.77.}Br_{0.27})_3$ absorber layer was passivated by the benzylamine molecules. The number of defects decreased, and the cell displayed an efficiency of 17.1%. The cells were stable even after four days under illumination and maintained 8% of their efficiency.

Table 3: Wide bandgap perovskite absorber layers in literature

Deposition Route	Absorber Layer	Efficiency	Bandgap	Reference
One-step spin coating	$FA_{0.83}Cs_{0.17}Pb(I_xBr_{1-x})_3$	17.1%	1.7-1.8 eV	[48]
One-step spin coating	$(FA_{0.83}MA_{0.17})_{0.95}Cs_{0.05}Pb(I_{0.6}Br_{0.4})_3$	18.5%	1.71 eV	[49]
One-step spin coating	$Cs_yFA_{1-y}Pb(I_xBr_{1-x})_3$	11.93%	-	[50]
One-step spin coating	$FA_{0.85}Cs_{0.15}PbI_{2,2}Br_{0.8}$	17.1%	1.72 eV	[51]
One step spin coating	$FA_{0.85}Cs_{0.15}Pb(I_{0.77.}Br_{0.27})_3$	17.1%	1.72 eV	[52]

Summary

Perovskites have an orthorhombic crystal structure with a cation, a metal ion and a halide one. They possess many attractive properties such as tunable bandgap, higher absorbance, better charge transport and longer charge diffusion length which make them a viable candidate for solar cells. However, they face challenges associated with stability, intrinsic defects and recombination losses. The selected deposition route has an important role with regards to the quality of the light absorbing layer. Solution processing techniques such as one-step spin coating, sequential deposition, vapor-based deposition and vacuum assisted solution processing are some common deposition methods. The standard perovskite solar cell is the methylammonium lead iodide having a bandgap of 1.55 eV. A higher bandgap falls under the category of wide bandgap solar cells which have proven to be a viable candidate for tandem architectures. The wide bandgap solar cells have achieved up to 18.5% efficiency on their own and can reach greater than 30% in tandem with other cells. All these cells are however, deposited using one-step spin coating even though sequential deposition influences the crystallization and leads to an improved quality of the film.

References

[1]   S. C. Watthage, Z. Song, A. B. Phillips, and M. J. Heben, "Evolution of Perovskite Solar Cells," in *Perovskite Photovoltaics*, Elsevier, 2018, pp. 43–88.

[2]   S. Demic, A. N. Ozcivan, M. Can, C. Ozbek, and M. Karakaya, "Recent Progresses in Perovskite Solar Cells," in *Nanostructured Solar Cells*, InTech, 2017.

[3]   G. Kieslich, S. Sun, and A. K. Cheetham, "An extended Tolerance Factor approach for organic-inorganic perovskites," *Chem. Sci.*, vol. 6, no. 6, pp. 3430–3433, Jun. 2015.

[4]   M. Saliba, J.-P. Correa-Baena, M. Grätzel, A. Hagfeldt, and A. Abate, "Perovskite Solar Cells: From the Atomic Level to Film Quality and Device Performance," *Angew. Chemie Int. Ed.*, vol. 57, no. 10, pp. 2554–2569, Mar. 2018.

[5]   W. J. Yin, J. H. Yang, J. Kang, Y. Yan, and S. H. Wei, "Halide perovskite materials for solar cells: A theoretical review," *J. Mater. Chem. A*, vol. 3, no. 17, pp. 8926–8942, May 2015.

[6]   K. Hwang *et al.*, "Toward Large Scale Roll-to-Roll Production of Fully Printed Perovskite Solar Cells," *Adv. Mater.*, vol. 27, no. 7, pp. 1241–1247, Feb. 2015.

[7]   "NREL Efficiency Chart."

[8]   T. Gatti, E. Menna, M. Meneghetti, M. Maggini, A. Petrozza, and F. Lamberti, "The Renaissance of fullerenes with perovskite solar cells," *Nano Energy*, vol. 41. Elsevier Ltd, pp. 84–100, 01-Nov-2017.

[9]   D. Cui *et al.*, "Color-Tuned Perovskite Films Prepared for Efficient Solar Cell Applications," *J. Phys. Chem. C*, vol. 120, no. 1, pp. 42–47, Jan. 2016.

[10]   J. Im, C. C. Stoumpos, H. Jin, A. J. Freeman, and M. G. Kanatzidis, "Antagonism between Spin–Orbit Coupling and Steric Effects Causes Anomalous Band Gap Evolution in the Perovskite Photovoltaic Materials $CH_3NH_3Sn_{1-x}Pb_xI_3$," *J. Phys. Chem. Lett.*, vol. 6, no. 17, pp. 3503–3509, Sep. 2015.

[11]   C. C. Stoumpos, C. D. Malliakas, and M. G. Kanatzidis, "Semiconducting Tin and Lead Iodide Perovskites with Organic Cations: Phase Transitions, High Mobilities, and Near-Infrared Photoluminescent Properties," *Inorg. Chem.*, vol. 52, no. 15, pp. 9019–9038, Aug. 2013.

[12]   H. L. Zhu and W. C. H. Choy, "Crystallization, Properties, and Challenges of Low-Bandgap Sn-Pb Binary Perovskites," *Sol. RRL*, vol. 2, no. 10, p. 1800146, Oct. 2018.

[13]   B. Conings *et al.*, "Intrinsic Thermal Instability of Methylammonium Lead Trihalide Perovskite," *Adv. Energy Mater.*, vol. 5, no. 15, p. 1500477, Aug. 2015.

[14] M. R. Ahmadian-yazdi, F. Zabihi, M. Habibi, and M. Eslamian, "Effects of Process Parameters on the Characteristics of Mixed-Halide Perovskite Solar Cells Fabricated by One-Step and Two-Step Sequential Coating," *Nanoscale Res. Lett.*, 2016.

[15] H. J. Snaith *et al.*, "Anomalous Hysteresis in Perovskite Solar Cells," *J. Phys. Chem. Lett.*, vol. 5, no. 9, pp. 1511–1515, May 2014.

[16] E. L. Unger *et al.*, "Hysteresis and transient behavior in current-voltage measurements of hybrid-perovskite absorber solar cells," *Energy Environ. Sci.*, vol. 7, no. 11, pp. 3690–3698, Nov. 2014.

[17] W. Tress, N. Marinova, T. Moehl, S. M. Zakeeruddin, M. K. Nazeeruddin, and M. Grätzel, "Understanding the rate-dependent J-V hysteresis, slow time component, and aging in CH 3 NH 3 PbI 3 perovskite solar cells: The role of a compensated electric field," *Energy Environ. Sci.*, vol. 8, no. 3, pp. 995–1004, Mar. 2015.

[18] J. P. Correa-Baena *et al.*, "Promises and challenges of perovskite solar cells," *Science*, vol. 358, no. 6364. American Association for the Advancement of Science, pp. 739–744, 10-Nov-2017.

[19] E. T. Hoke, D. J. Slotcavage, E. R. Dohner, A. R. Bowring, H. I. Karunadasa, and M. D. McGehee, "Reversible photo-induced trap formation in mixed-halide hybrid perovskites for photovoltaics," *Chem. Sci.*, vol. 6, no. 1, pp. 613–617, Jan. 2015.

[20] T. Jesper Jacobsson *et al.*, "Exploration of the compositional space for mixed lead halogen perovskites for high efficiency solar cells," *Energy Environ. Sci.*, vol. 9, no. 5, pp. 1706–1724, May 2016.

[21] A. Mourtada Elseman, "Organometal Halide Perovskites Thin Film and Their Impact on the Efficiency of Perovskite Solar Cells," in *Coatings and Thin-Film Technologies*, IntechOpen, 2019.

[22] M. M. Rashad, A. M. Elseman, and A. M. Hassan, "Facile synthesis, characterization and structural evolution of nanorods single-crystalline (C4H9NH3)2PbI2X2 mixed halide organometal perovskite for solar cell application," *Optik (Stuttg).*, vol. 127, no. 20, pp. 9775–9787, Oct. 2016.

[23] J. T. W. Wang *et al.*, "Low-temperature processed electron collection layers of graphene/TiO 2 nanocomposites in thin film perovskite solar cells," *Nano Lett.*, vol. 14, no. 2, pp. 724–730, Feb. 2014.

[24] Y. Yang *et al.*, "Low-temperature solution-processed perovskite solar cells with high efficiency and flexibility," *ACS Nano*, vol. 8, no. 2, pp. 1674–1680, Feb. 2014.

[25] D. B. Mitzi, "Thin-film deposition of organic-inorganic hybrid materials," *Chemistry of*

Materials, vol. 13, no. 10. American Chemical Society , pp. 3283–3298, 2001.

[26] K. Liang, D. B. Mitzi, and M. T. Prikas, "Synthesis and Characterization of Organic-Inorganic Perovskite Thin Films Prepared Using a Versatile Two-Step Dipping Technique," *Chem. Mater.*, vol. 10, no. 1, pp. 403–411, 1998.

[27] L. K. Ono, M. R. Leyden, S. Wang, and Y. Qi, "Organometal halide perovskite thin films and solar cells by vapor deposition," *Journal of Materials Chemistry A*, vol. 4, no. 18. Royal Society of Chemistry, pp. 6693–6713, 03-May-2016.

[28] B. S. Kim, T. M. Kim, M. S. Choi, H. S. Shim, and J. J. Kim, "Fully vacuum-processed perovskite solar cells with high open circuit voltage using MoO3/NPB as hole extraction layers," *Org. Electron.*, vol. 17, pp. 102–106, Feb. 2015.

[29] O. Malinkiewicz *et al.*, "Metal-Oxide-Free Methylammonium Lead Iodide Perovskite-Based Solar Cells: The Influence of Organic Charge Transport Layers," *Adv. Energy Mater.*, vol. 4, no. 15, Oct. 2014.

[30] Q. Chen *et al.*, "Controllable self-induced passivation of hybrid lead iodide perovskites toward high performance solar cells," *Nano Lett.*, vol. 14, no. 7, pp. 4158–4163, Jul. 2014.

[31] R. Sheng *et al.*, "Methylammonium lead bromide perovskite-based solar cells by vapor-assisted deposition," *J. Phys. Chem. C*, vol. 119, no. 7, pp. 3545–3549, Feb. 2015.

[32] T. Du, N. Wang, H. Chen, H. Lin, and H. He, "Comparative study of vapor- and solution-crystallized perovskite for planar heterojunction solar cells," *ACS Appl. Mater. Interfaces*, vol. 7, no. 5, pp. 3382–3388, Feb. 2015.

[33] J. L. Barnett, V. L. Cherrette, C. J. Hutcherson, and M. C. So, "Effects of Solution-Based Fabrication Conditions on Morphology of Lead Halide Perovskite Thin Film Solar Cells," *Adv. Mater. Sci. Eng.*, vol. 2016, 2016.

[34] Y. Zhao, J. Liu, X. Lu, Y. Gao, X. You, and X. Xu, "Improving the efficiency of perovskite solar cells through optimization of the CH 3 NH 3 PbI 3 film growth in solution process method," *Appl. Surf. Sci.*, vol. 359, pp. 560–566, Dec. 2015.

[35] Y. Xu *et al.*, "The Effect of Humidity upon the Crystallization Process of Two-Step Spin-Coated Organic-Inorganic Perovskites," *ChemPhysChem*, vol. 17, no. 1, pp. 112–118, Jan. 2016.

[36] Q. Chen *et al.*, "Planar heterojunction perovskite solar cells via vapor-assisted solution process," *J. Am. Chem. Soc.*, vol. 136, no. 2, pp. 622–625, Jan. 2014.

[37] L. Zhou *et al.*, "Enhanced planar perovskite solar cell efficiency and stability using a perovskite/PCBM heterojunction formed in one step," *Nanoscale*, vol. 10, no. 6, pp.

3053–3059, Feb. 2018.

[38] L. Etgar, P. Gao, Z. Xue, Q. Peng, A. K. Chandiran, and B. Liu, "Mesoscopic CH 3 NH 3 PbI 3 /TiO 2 Heterojunction Solar Cells," pp. 8–11, 2012.

[39] M. Gra, "Sequential deposition as a route to high-performance perovskite-sensitized solar cells," pp. 4–8.

[40] S. Kulkarni, "Improved light absorption and charge transport for perovskite solar cells with rough interfaces by sequential deposition," pp. 8171–8176, 2014.

[41] M. Liu, M. B. Johnston, and H. J. Snaith, "Efficient planar heterojunction perovskite solar cells by vapour deposition," *Nature*, vol. 501, no. 7467, pp. 395–398, Sep. 2013.

[42] D. Forgács *et al.*, "Efficient Monolithic Perovskite/Perovskite Tandem Solar Cells," *Adv. Energy Mater.*, vol. 7, no. 8, pp. 1–6, 2017.

[43] Q. Chen *et al.*, "Planar heterojunction perovskite solar cells via vapor-assisted solution process," *J. Am. Chem. Soc.*, vol. 136, no. 2, pp. 622–625, Jan. 2014.

[44] H. Zhou, Q. Chen, and Y. Yang, "Vapor-assisted solution process for perovskite materials and solar cells," *MRS Bull.*, vol. 40, no. 8, pp. 667–673, Aug. 2015.

[45] M. T. Hörantner *et al.*, "The Potential of Multijunction Perovskite Solar Cells," *ACS Energy Lett.*, vol. 2, no. 10, pp. 2506–2513, Oct. 2017.

[46] Z. Song, C. Chen, C. Li, R. A. Awni, D. Zhao, and Y. Yan, "Wide-bandgap, low-bandgap, and tandem perovskite solar cells," *Semiconductor Science and Technology*, vol. 34, no. 9. Institute of Physics Publishing, 29-Jul-2019.

[47] M. Kot, M. Vorokhta, Z. Wang, H. J. Snaith, D. Schmeißer, and J. I. Flege, "Thermal stability of CH3NH3PbIxCl3-x versus [HC(NH2)2]0.83Cs0.17PbI2.7Br0.3 perovskite films by X-ray photoelectron spectroscopy," *Appl. Surf. Sci.*, vol. 513, p. 145596, May 2020.

[48] D. P. McMeekin *et al.*, "A mixed-cation lead mixed-halide perovskite: The ideal absorber for tandem solar cells," *Science (80-.).*, vol. 351, no. 6269, p. accepted, 2016.

[49] Y. Lin, B. Chen, F. Zhao, X. Zheng, Y. Deng, and Y. Shao, "Matching Charge Extraction Contact for Wide-Bandgap Perovskite Solar Cells," vol. 1700607, pp. 1–8, 2017.

[50] R. Szostak and E. Marchezi, "Sustainable Energy & Fuels Exploring the formation of formamidinium-based hybrid perovskites by antisolvent methods : in situ GIWAXS measurements during spin coating †," 2019.

[51] Y. Zhou *et al.*, "Composition-Tuned Wide Bandgap Perovskites: From Grain Engineering to Stability and Performance Improvement," *Adv. Funct. Mater.*, vol. 28,

no. 35, pp. 1–8, 2018.

[52]   Y. Zhou *et al.*, "Benzylamine-Treated Wide-Bandgap Perovskite with High Thermal-Photostability and Photovoltaic Performance," *Adv. Energy Mater.*, vol. 7, no. 22, pp. 4–10, 2017.

Chapter 3: Introduction to Fabrication and Characterization Techniques

3.1 Rotary Evaporator

Rotary evaporators also known as 'rotovaps' are used to recover solvents and evaporate excess liquid from reaction mixtures. They are usually found in organic chemistry labs since they are mostly used for organic mixtures. The equipment has the capacity to handle a substantial volume of 3 liters. Typically, the rotary evaporator comes with a water bath for indirect heating of the mixture to be evaporated and prevent it from freezing. The evaporation is performed under vacuum and its vapors are trapped in a condenser coil which collects it in a flask. A simple water aspirator can be used to create vacuum when the materials are not air or moisture sensitive. The purpose of using the vacuum is to significantly lower the boiling points of solvent.

Figure 7: Labelled diagram of a rotary evaporator setup [1]

The flask with the reaction mixture is rotated during the procedure to increase the surface area and hence the evaporation rate. The evaporated solvent is collected and can be either reused or disposed. Since lower temperatures are used, the method prevents the compound from overheating or oxidizing [2].

3.2 Spin Coating

Spin coating is a common deposition technique for thin film application. It is employed in a plethora of applications in many industries. The advantages of spin coating are that it is easy, quick and capable of producing uniform films of thickness ranging from nanometers to a few microns. [3]

Working Principle
The technique requires the deposition of a thin film on the substrate surface by casting a solution containing the compound dissolved in solvent and rotating it at low or high speeds. The step-by-step procedure is given as:

1. Substrate is covered with the solution with the desired material dissolved in a compatible solvent
2. High seed rotation of the substrate allows most of the solvent to fly off to the sides
3. The substrate is dried to evaporate the remaining solvent and obtain a layer of the desired molecules.

At high rotations seeds (up to 12,000 rpm) the centripetal force coupled with the surface tension associated with the solution and substrate interface pulls the coating to all sides resulting in even coverage. The solvent also evaporates during the sinning and the film is further annealed to completely dry it off.

(i) Deposition

(ii) Spin up

(iii) Spin off

(iv) Evaporation
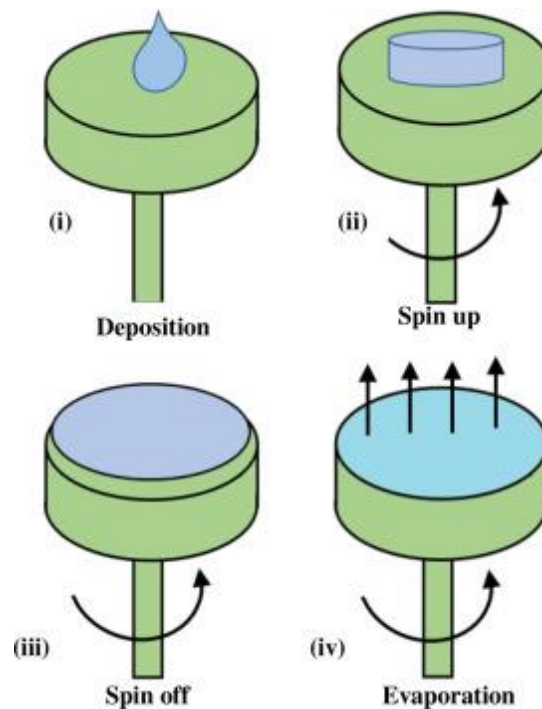
Figure 8: Spin coating mechanism [4]

39

Thickness Equation

The thickness of the spin-coated film depends on the spin seed and angular velocity. The thickness is inversely proportional to the revolutions per minute at which the substrate is rotated.

$$t \propto \frac{1}{\sqrt{\omega}}$$

where

t is the layer's thickness

w is the angular velocity

3.3 Glove Box

Glove boxes are used by radiochemical, metallurgical and fabrication laboratories. It consists of a safety glass screen for visibility and vacuum sealed gloves for safe handling of materials inside the box. [5]

Figure 9: Glove box

A glove box can be compared to a fume hood except that it has an exhaust system, and the inside environment is strictly controlled. The box is completely closed to prevent air from entering and there are only arm-length gloves to allow experiments to be performed within the equipment. An inert gas like argon and nitrogen can be used to bring down the oxygen and

moisture level to less than 0.1 ppm A purifier or filter is fitted inside the glove box to recycle the gas maintain an inert environment [6].

3.4 UV-Visible Spectroscopy

Ultraviolet visible spectroscopy (UV-Vis) is a very popular characterization technique because of its ability to detect almost every molecule. Light in the ultraviolet to visible region illuminates the sample and the amount of light passed through is recorded. This gives us the transmittance behavior of the material and by a simple calculation, the absorbance can also be analyzed. The amount of light absorbed or transmitted at a given wavelength gives us information about the chemical structure of the material under investigation [6].
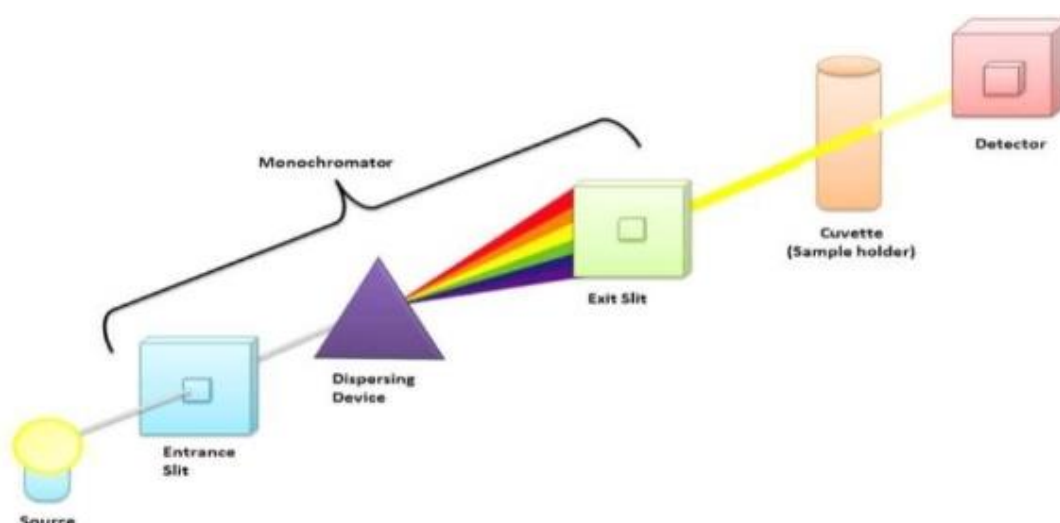
Figure 10: Instrumentation of a UV-Vis Spectrophotometer

The technique is often used for general analysis because most elements and compounds can absorb light in that range. The wavelength range for the light used extends from 100 nm (deep UV) to 1000 nm (beyond visible). For this long range of light, typically two different sources are used. The deuterium lamp is for the UV light whereas a tungsten filament produces visible light.

Working Principle

A photon strikes the molecule and after being absorbed excites the molecule to a higher energy state. The UV-Visible light has high energy with the ability to transfer electrons from the highest occupied orbital to an excited state in the lowest unoccupied orbital. The different in energy between both states is the bandgap of the material. The bandgap is unique for each material therefore every crystal structure has its own characteristic absorption spectra.

3.5 Scanning Electron Microscopy

The scanning electron microscope is an imaging technique that focuses a beam of electrons to produce signals from the surface of a solid sample. The way the electron interacts with the specimen reveals information about it including the texture, morphology, chemical composition, orientation and crystal structure of the materials resent in the sample [7].

A 2-dimensional image of a selected area of the surface is generated using the camera. For conventional equipment, the area can vary from 1 cm to 5 µm width using the scanning mode. The magnification range is from 20x up to 30,000x.

Working Principle

The electrons are accelerated and the kinetic energy they possess is converted into signals when these electrons interact with the sample. The decelerated electrons generate secondary and backscattered electrons when they strike the solid sample. The electrons are responsible for producing the SEM images while the Bremsstrahlung X-rays provide crystal structure data.

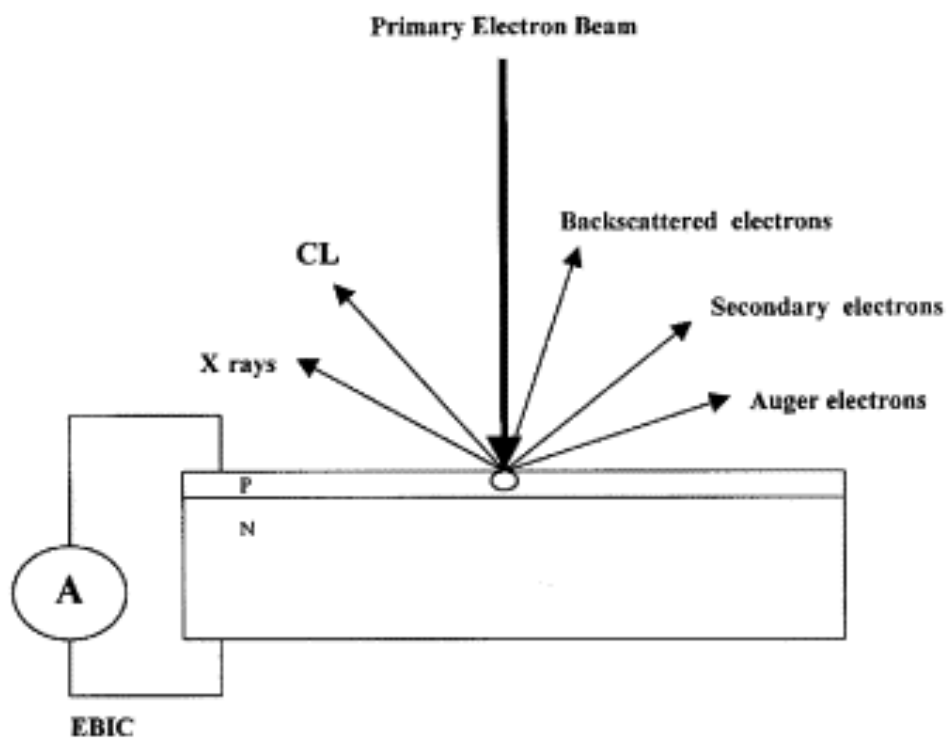*Figure 11: Electron-surface interaction within a SEM* [8]

The SEM can also give us information on the chemicals present in the sample by analyzing the x-rays produced due to inelastic collision of the electron with the element orbital. When the excited electron deexcites and returns to its orbital it releases an X-ray of characteristic wavelength that is useful for identifying the chemical composition of the sample.

3.6 X-ray Diffraction

X-ray diffraction is a nondestructive characterization technique applied for the analysis of crystalline materials. XRD can give us information on the crystal structure, phases, orientations and other crystal lattice parameters. We can also determine the grain size, micro strain and presence of crystal defects. The diffraction peaks are generated due to constructive interference of the X-ray beams at particular angles from each lane of the crystal lattice in a sample [9].

Working Principle

X-ray diffraction is a result of the elastic scattering of photons by the periodic crystal lattice. The in-phase monochromatic X-rays constructively interfere after reflecting of the crystal plane. The lattice spacing is then derived using Bragg's law.
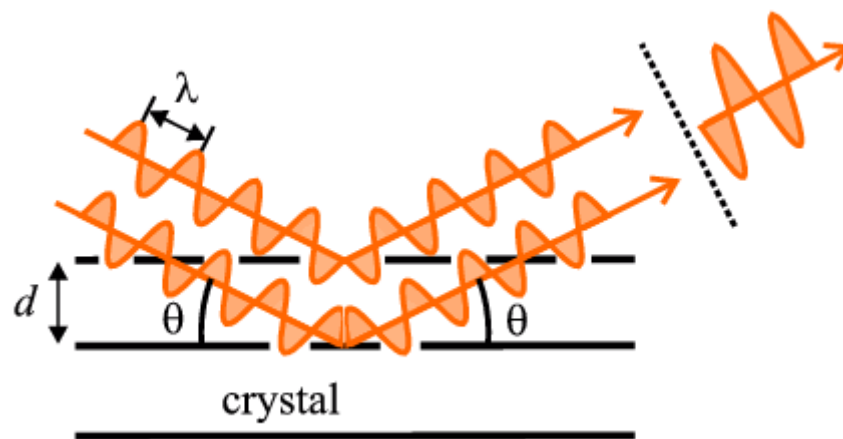
Figure 12: Constructive interference on a crystal plane

$$n\lambda = 2d \sin\theta$$

where

n is the order of reflection

λ is the x-ray light wavelength

d is the spacing that separates two different planes in a crystal lattice

θ is the angle difference between the incident ray and the plane normal

The θ angles at which the x-rays are leaving the crystal plane are measured and the interplanar d-spacing can be determined from that. An unknown substance can also be identified using XRD, by matching the θ values at different intensities with standard patterns available in online databases.

3.7 Atomic Force Microscopy

Atomic Force Microscopy or AFM is a surface analysis technique which is useful for studying coatings at a micro or nano scale. The microscopy can be used to obtain images at a nanoscale range to study the air or liquid sample. The AFM can be used for high resolution imaging of many different surfaces to determine surface morphology, roughness and texture. The tip senses the chemical atoms by forming chemical bonds with them. The interactions alter the vibrational frequency and these changes are mapped out by the program [10].

Working Principle

AFM uses a sharp tip with a diameter of around 10 to 20 nm to measure the surface's properties. A cantilever is attached to the tip which is made of silicon or silicon nitride. The movement of the tip is recorded by a laser beam emitted by a photodiode.
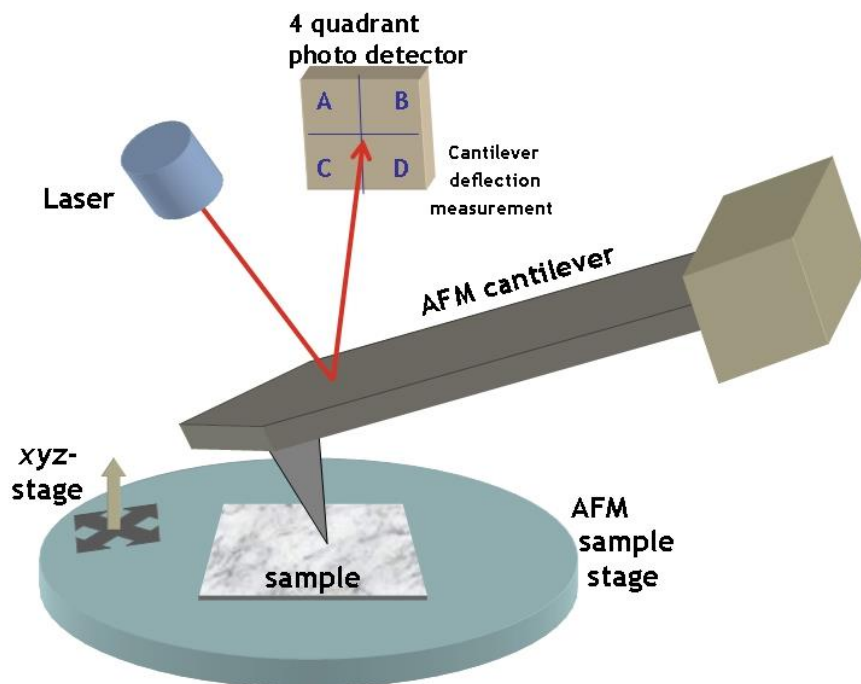
Figure 13: An Atomic Force Microscope setup

The equipment operates in two different modes i.e., the tapping and contact mode. The AFM tip and the surface are in constant contact during the contact mode. This measurement mode is only for specific applications such as that of the force curve. For the tapping mode, the cantilever moves to allow only brief contact of the tip with the sample. This process eliminates any shear forces associated with the moving tip. It is the recommended mode of operation for standard AFM imaging [11].

3.8 Profilometry

A profiler is an instrument which is to characterize the topography of the uppermost layers of a film and measure its overall thickness. It has multiple points which measure the variation in the texture of a surface at the sub-micron level. The analysis is used to determine the surface roughness and fractality [12].

Working Principle

Figure 14: A non-contact profilometer

Non-contact surface profilometers utilize a range of optical techniques to find out information about a surface's topography. An incident light source illuminates the surface during scanning. It measures the reflective, refractive and emissive light to put together information about the surface topography. This method is preferred over the contact profilers because it is not invasive and offers faster measurement.

Summary

Rotary evaporators are used to remove excess solvents from a solution, and they can effectively lower the boiling point of the liquid by creating a pressure. It reduces the boiling time and protects the solution from high temperatures.

A spin coater is used to cast a solution on to a substrate for thin film deposition. It rotates at high speeds to allow the solution to fly off and spread evenly on the substrate. The layer thickness is dependent on the rotational speed.

A glove box separates the user from the environment inside by a glass screen. The environment within the box is highly controlled and uses inert gases such as argon or nitrogen to remove the air particles.

Ultraviolet-visible (UV-Vis) spectroscopy uses ultraviolet to visible light to determine the chemical makeup of the material being characterized. The amount of light that is transmitted or absorbed gives us information about the molecules in the sample.

The scanning electron microscope is a powerful imaging tool that employs a beam of electron to produce signals from the surface of a sample. The electron interactions give us insight into the morphology, grain size, orientation and composition of the materials present in the sample.

The X-ray diffraction uses X-rays at different angles and measures the diffraction peaks from constructive interference to determine information about the crystallinity of an object. It helps us find the crystal size, orientation, phases and lattice parameters along with other useful information.

An atomic force microscope uses a silicon or silicon nitride tip to measure the surface topography and morphology. The tip is mostly used in the tapping mode where merely a brief contact with the surface determines the surface properties by reading the chemical bonds of the tip with the surface.

A profilometer measures the surface roughness and thickness using an optical source to measure the reflective, refractive angles of light. It is a fast, non-contact procedure.

References

[1]   "Rotary Evaporator." [Online]. Available: https://www.pro-lab-direct.com/product-p/ple1000.htm. [Accessed: 15-Dec-2019].

[2]   "How to use a Rotary Evaporator." [Online]. Available: http://www.chem.ucla.edu/~bacher/Specialtopics/rotavap.html. [Accessed: 13-Dec-2019].

[3]   "Spin Coating, A Complete Guide to Theory and Techniques | Ossila." [Online]. Available: https://www.ossila.com/pages/spin-coating. [Accessed: 13-Dec-2019].

[4]   "Spin Coating - an overview | ScienceDirect Topics." [Online]. Available: https://www.sciencedirect.com/topics/materials-science/spin-coating. [Accessed: 15-Dec-2019].

[5]   "Glove Box - an overview | ScienceDirect Topics." [Online]. Available: https://www.sciencedirect.com/topics/engineering/glove-box. [Accessed: 13-Dec-2019].

[6]   "Ultraviolet-Visible (UV-Vis) Spectroscopy | Protocol." [Online]. Available: https://www.jove.com/science-education/10204/ultraviolet-visible-uv-vis-spectroscopy. [Accessed: 13-Dec-2019].

[7]   "Scanning Electron Microscopy (SEM)." [Online]. Available: https://serc.carleton.edu/research_education/geochemsheets/techniques/SEM.html. [Accessed: 13-Dec-2019].

[8]   "Scanning Electron Microscope - an overview | ScienceDirect Topics." [Online]. Available: https://www.sciencedirect.com/topics/neuroscience/scanning-electron-microscope. [Accessed: 15-Dec-2019].

[9]   "X-Ray Diffraction - an overview | ScienceDirect Topics." [Online]. Available: https://www.sciencedirect.com/topics/materials-science/x-ray-diffraction. [Accessed: 13-Dec-2019].

[10]   M. Aliofkhazraei and N. Ali, "AFM Applications in Micro/Nanostructured Coatings," in *Comprehensive Materials Processing*, vol. 7, Elsevier Ltd, 2014, pp. 191–241.

[11]   S. Sinha Ray, "Techniques for characterizing the structure and properties of polymer nanocomposites," in *Environmentally Friendly Polymer Nanocomposites*, Elsevier, 2013, pp. 74–88.

[12]   "What is a Surface Profiler | Profilometer Working Principle." [Online]. Available: https://www.taylor-hobson.com/resource-center/blog/2018/july/what-is-a-surface-

profiler. [Accessed: 08-Aug-2020].

Chapter 4: Experimental Procedure

4.1 Materials Used

The formamidine acetate salt (CAS No. 3473-63-0), lead iodide salt (CAS No 10101-63-0), cesium bromide salt (CAS No. 7787-69-1), formamidnium bromide salt (CAS No. 146958-06-7) and FTO coated glass (EC No. 242-159-0) were purchased from Sigma Aldrich. The hydroiodic acid was bought from Alfa Aesar (CAS No. 10034-85-2).

4.2 Formamidinium Iodide Synthesis

The formamidinium iodide was synthesized using a method adapted from the literature with modifications [1]. 2 molar excess of formamidine acetate salt was stirred into 10ml of methanol over an ice bath. 57% w/w hydroiodic acid was added into the flask drop-wise under constant stirring and then left to stir at 0°C for two hours. The solvents were carefully evaporated using a rotary evaporator at 75-80°C for five hours. After evaporation a precipitate was left behind which was then washed with excess amounts of diethyl ether until it was off-white in colour. We dehydrated the crystals in a vacuum oven at 60°C for 24 hours before using them.

Figure 15: R to L: FAI crystals before washing and FAI crystals after washing with diethyl ether

4.3 Substrate Cleaning Procedure

The glass and FTO-coated glass slides were kept in a mild detergent solution and then sonicated for 15 minutes. After rinsing with deionized water, the slides were sonicated in isopropyl alcohol, acetone then isopropyl alcohol sequentially for 15 minutes each. They were dried in air and heated on a hot plate at 70 degrees before spincoating.

4.4 Perovskite Absorber Layer Deposition

We prepared a 1M solution of PbI_2 using 461 mg of PbI_2 and mixing it in 1 ml of DMSO and DMF with a 2:3 ratio. The solution was stirred for 1 hour at 70 degrees and kept at that temperature during the spincoating procedure. The solution was spincoated onto the glass and FTO glass substrates at 2000 rpm for 25 s. The films were dried on a hot plate at 70 °C for 10 mins.

Figure 16 PbI2 films after deposition and annealing

The slides were then shifted to a globebox and dip coated in a solution of CsBr, FAI and FABr in IPA to achieve varying ratios. For example 0.2 mM of CsBr, 0.5 mM of FAI and 0.5 mM of FABr was used for $FA_{0.8}Cs_{0.2}PbI_{2.5}Br_{0.5}$. The composition of Br was kept at 0, 0.3, 0.5, 0.7 and 1. The table given below lists the quantities of precursor salts used to achieve each one of the compositions that were a part of this research.

Table 4: Quantities of salts used in dipping precursor solution

Composition	FAI (mg/10ml)	CsBr (mg/10ml)	FABr(mg/10ml)
FAPbI$_3$	16.00	0.00	0.00
FA$_{0.8}$Cs$_{0.2}$PbI$_{2.7}$Br$_{0.3}$	11.20	4.26	1.13
FA$_{0.8}$Cs$_{0.2}$PbI$_{2.5}$Br$_{0.5}$	8.00	4.26	3.39
FA$_{0.8}$Cs$_{0.2}$PbI$_{2.3}$Br$_{0.7}$	4.80	4.26	5.65
FA$_{0.8}$Cs$_{0.2}$PbI$_2$Br	0.00	4.26	9.04

4.4.1 Dipping Time

Initially the PbI$_2$ layers were dipped in the CsBr and FAI solution for only 60 seconds because the literature on sequentially deposited MAPbI$_3$ films suggested longer dipping times can cause poorer film coverage and lead to the formation of shunt pathways in the absorber layer [2]. However, experiments involving Br required a longer dipping time for complete conversion of the perovskite layer [3] so it was increased to 15 mins. This was followed by drying on a hot plate at 120 °C for 30 minutes.

4.5 Characterization

4.5.1 X-ray Diffraction

For the structural investigation and crystal size analysis of the perovskite films, the X-ray Diffraction (XRD) technique was used through the Bruker, D8 Advanced with a scanning rate of 1.2/min and 2θ in the range of 5° to 70°. The XRD used a CuKα radiation source (λ=1.54056 Å) generated at an excitation voltage 40 kV and current 40 mA. MDI Jade 6.5 was used for the peak analysis, hkl determination and signal processing.

4.5.2 Scanning Electron Microscopy

The surface morphology of the layer was captured using the Scanning Electron Microscope (SEM). For the scanning a MIRA3 TESCAN was used. The images were recorded for 10.0 Kx magnification and a voltage of 10.0 KV was set for the scans.

4.5.3 UV-Vis Spectrophotometry

To study the film's optical properties, the UV-Vis NIR Spectrophotometer UV-3600 Plus was used. The asborbance of the samples was measured in the range of 300 to 1100 nm with a slit width of 2.5 μm.

4.5.4 Atomic Force Microscopy

The surface topography and roughness was investigated using the Atomic Force Microscopy technique. A Nanosurf FlexAFM Version 5 was used in static mode. The feature size was kept at 2.5 µm and the expected height was 1.5 µm. The images were analyzed and processed using the Gwyddion software.

4.5.5 Non-contact Profilometer

The film thickness was recorded using a 2D Optical Profilometer. It was a non-contact instrument PS-50 from Nanovea. A scanning length of 12 mm was used to measure the average height of the film.

All measurements and characterizations were carried out ex-situ.

Summary

The experimental procedure involved the synthesis of formamidinium iodide using formamidine acetate salt and hydrioiodic acid. The salt and acid were combined using methanol as a reagent and the resultant formaidnium iodide was recovered using a rotary evaporator. We performed the absorber layer deposition on a FTO coated glass substrate which was cleaned prior to spincoating using dish washing liquid, acetone and isopropanol. The substrates were preheated at 70°C before deposition. A 1M lead iodide solution was spincoated onto the substrate at 2000 rpm for 25 seconds. The films were heated on a hot plate at 70°C to evaporate the excess solvent. They were shifted into a glove box for the dip coating step. The substrates were dipped in a solution of formamidinium iodide, cesium bromide and cesium iodide in various ratios to achive the desired composition. A dipping time of 15 minutes was selected for complete layer formation and the substrates were dried at 120°C after it. The layers were characterized using XRD, SEM, AFM, UV-Vis Spectrophotometer and non-contact profilometer.

References

[1]   T. M. Koh *et al.*, "Formamidinium tin-based perovskite with low Eg for photovoltaic applications," *J. Mater. Chem. A*, vol. 3, no. 29, pp. 14996–15000, Jul. 2015.

[2]   M. R. Ahmadian-yazdi, F. Zabihi, M. Habibi, and M. Eslamian, "Effects of Process Parameters on the Characteristics of Mixed-Halide Perovskite Solar Cells Fabricated by One-Step and Two-Step Sequential Coating," *Nanoscale Res. Lett.*, 2016.

[3]   S. A. Kulkarni, T. Baikie, P. P. Boix, N. Yantara, and N. Mathews, "Band-gap tuning of lead halide perovskites using a sequential," 2014.

Chapter 5: Results and Discussion

5.1 Dipping Time Effect

The dipping time of the PbI_2 films was varied from 60 seconds to 15 minutes because it was suggested in the literature that perovskite layers involving Br require longer dipping times [1]. According to the UV-Vis spectroscopy results shown in Fig. 17(a), a longer dipping time resulted in a higher absorbance of the film. This can be attributed to the complete conversion of the perovskite and improved crystallinity as shown in Fig. 17(b). The film prepared by dipping for 60 secs in the precursor solution shows a strong presence of PbI_2 peaks. The suppression of these peaks and the larger perovskite phase peaks points towards a more crystalline perovskite structure with very little residual PbI_2. The absorbance also increased as the CsBr content in the film is increased since the presence of Cs promotes the crystallization of the film [2]. The absorbance curves observed for these films tend to be flat which could also be due to the larger crystal size and higher thickness of the film [3]. All the following samples were fabricated using a dipping time of 15 minutes.
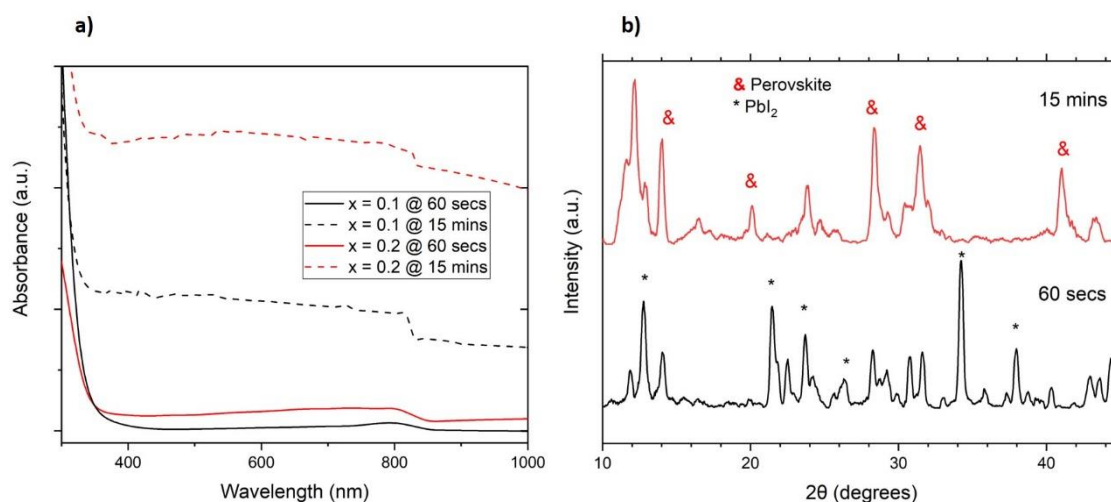

Figure 17(a): Absorbance curves for the $FA_{1-x}Cs_xPbI_{3-x}Br_x$ perovskite layers where x represents the molar ratio of CsBr used.(b) XRD pattern for samples after increasing dipping time from 60 secs to 15 mins.
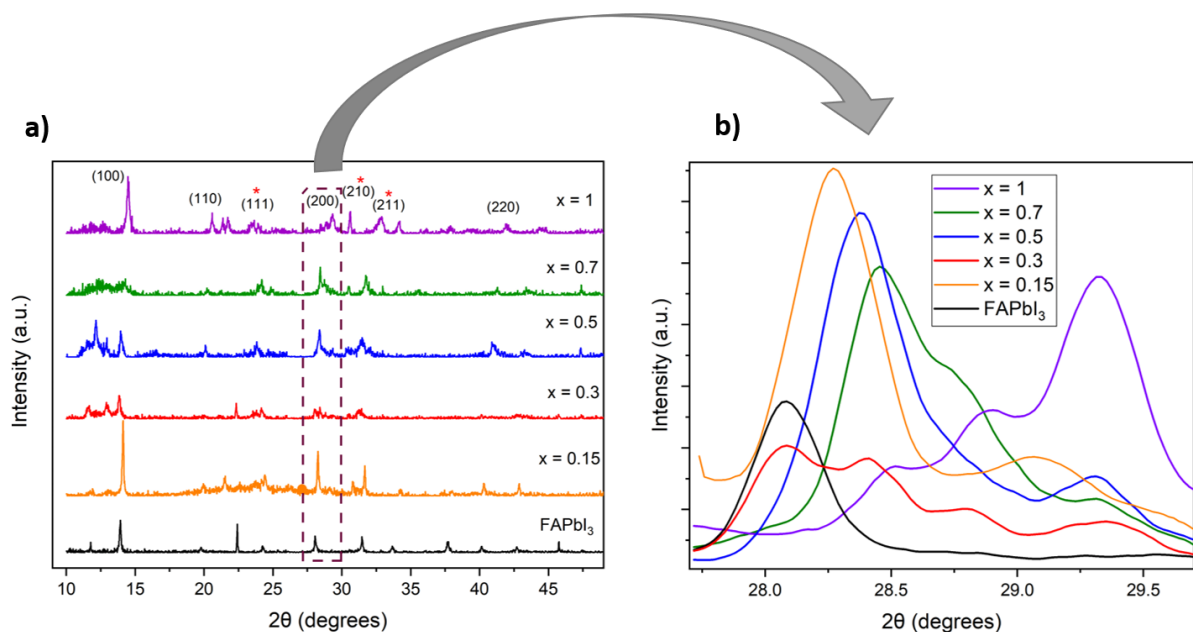
5.2 XRD Analysis

Figure 18(a): XRD pattern for the FAPbI₃ and FA₀.₈Cs₀.₂PbI₃₋ₓBrₓ perovskite layers labelled by the concentration of Br used. The hkl indices labelled in black correspond to the characteristic perovskite phase, while those in red are the CsPbBr₃ peaks.(b) XRD pattern magnified at the 28° peak.

The XRD patterns for the different film compositions are shown in Fig. 18(a). The characteristic perovskite peaks at 14° (100), 20° (110), 28° (200), 40° (220) become more prominent and shift to larger angles as the Br content is gradually increased. However, the PbI_2 peak at 12° remains present throughout the different compositions showing the incomplete conversion of the perovskite layer and the presence of remnant PbI_2 film. There is also the presence of another prominent phase in the Br 0.5, 0.7, and 1 film, which is visible at 24° (111), 30° (210), and 34° (211). These values match with the $CsPbBr_3$ perovskites, and it seems that only the CsBr is incorporating itself into the lattice while the FAI and FABr are being rejected. The ionic radius of Cs (179 pm) is smaller than that of FA (250 pm), which could be the reason it is easily inserted into the structure.

Fig. 18(b) shows a magnification of the XRD peak around 28°. The signal has been processed, so the relative height of the peak does not depict the actual intensity. However, as it is visible from the graph, the peak shifts to a larger angle as the ratio of Br is increased. The peak observes a monotonic shift from 28.2° for FAPbI₃ to 29.6° for Br-1. This is characteristic of shrinkage of the lattice and a reduction in crystal size. As more and more of Br is added to the ratio, the I is replaced. Since Br⁻ has a smaller ionic radius than I⁻ it causes the lattice to contract. These claims can be supported by what has already been reported in the literature [4], [5].

Additionally, it is interesting to note that the relative intensity increases as more Br is added to the precursor, which shows a more ordered and crystalline perovskite phase [6].
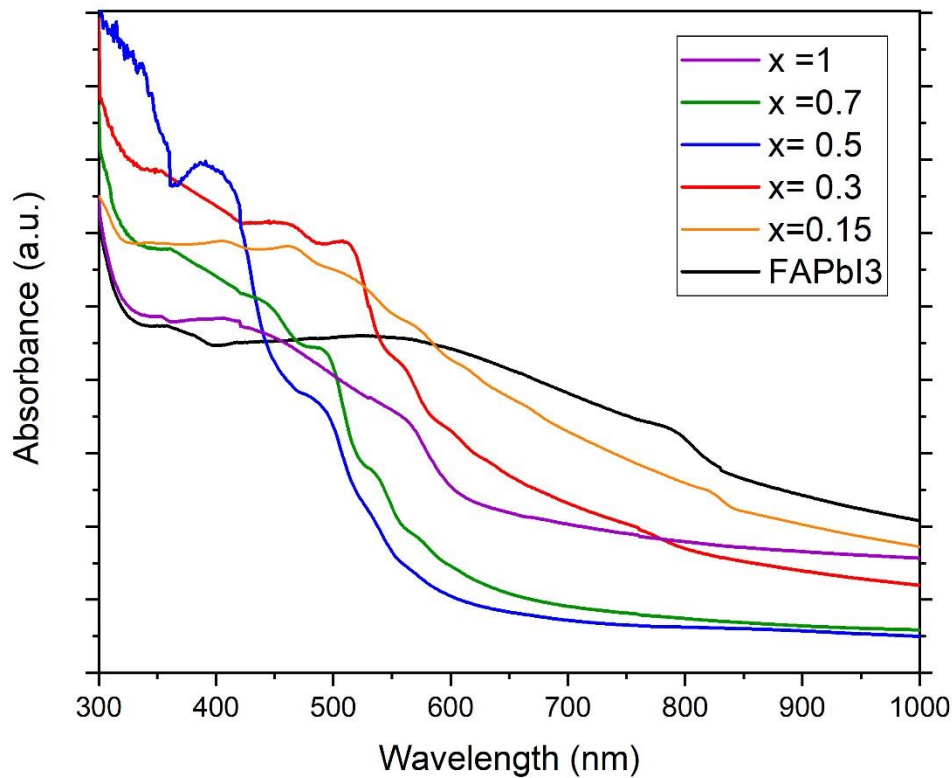
5.3 Optical Properties

Figure 19: Absorbance curves for the FAPbI$_3$ and FA$_{0.8}$Cs$_{0.2}$PbI$_{3-x}$Br$_x$ perovskite layers

The absorbance graph for the FAPbI$_3$ sample has an absorption onset around 830 nm which corresponds to the bandgap of 1.49 eV as reported in the literature [7]. When the bandgap was calculated through a Tauc plot using the thickness of 1μm obtained from the profilometry, it was 1.52 eV. The same value was obtained for the Br-0.15 sample. The Br-0.3 absorbance is blue shifted and has a bandgap of 1.83 eV. However, as the percentage of Br is increased, the absorbance curves are greatly blue shifted. The bandgap increases to greater than 2eV for Br-0.5 and Br-0.7. It is closer to a bandgap of CsPbBr$_3$ which has been reported to be 2.3 eV. In the absorbance graph there is a distinct absorption edge around 500 nm which is characteristic of CsPbBr$_3$ [8]. This corroborates the presence of the CsPbBr$_3$ peaks in the XRD pattern and proves that the FA cation is not being included in all the perovskite crystal structure. The CsBr salt proves to be more dominant and the reason for that is the seven-times higher complexation

constant between the Pb-Br species [9], [10]. The higher affinity of Pb^{2+} towards Br^{-} ion leads to the I^{-} ion playing the role of a spectator. The Br-1 film, however, has a lower bandgap of 2 eV and the absorption onset is also red-shifted because a higher concentration of FABr was used to achieve this composition and therefore FA was included in the perovskite structure. As inferred in the literature, the sharp increase in absorbance shows that the samples' crystallinity improves by adding more Br [2].
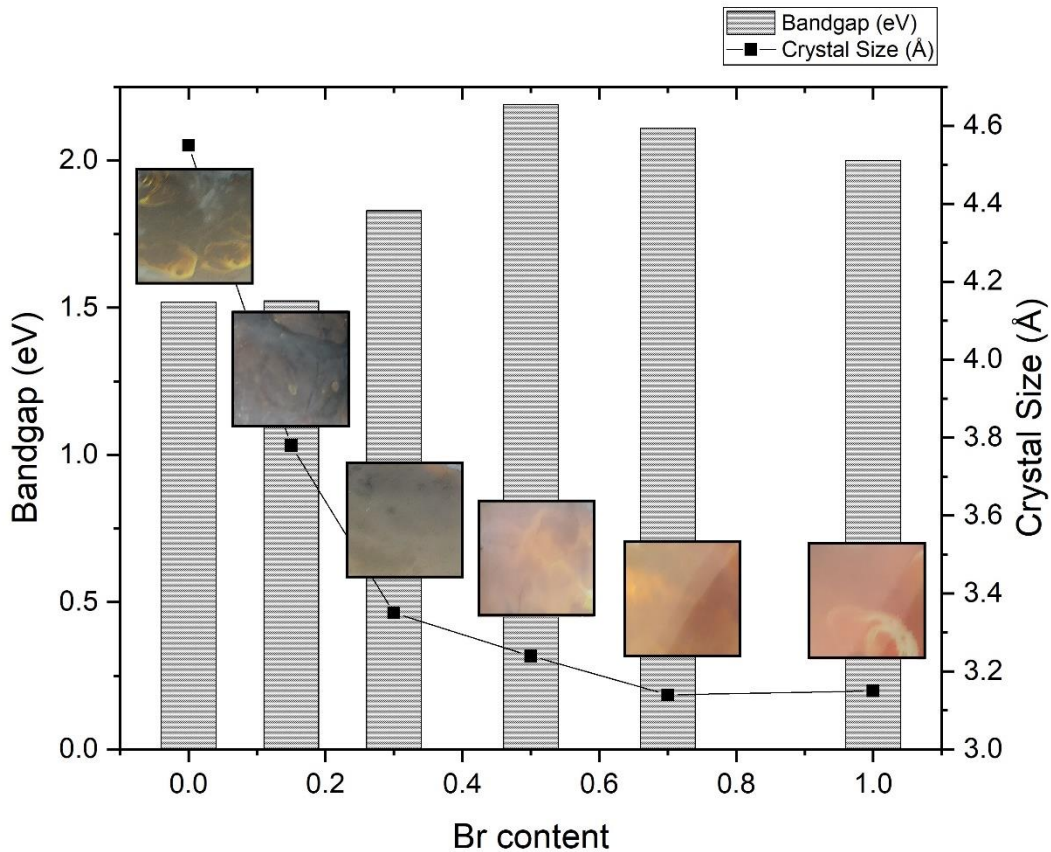
Figure 20: Relationship between the Br concentration, crystal size and bandgaps of the $FA_{0.8}Cs_{0.2}PbI_{3-x}Br_x$ perovskites. The insets show photographs in top view of the films taken after deposition.

The crystal size of the different layers was calculated by analyzing the peaks from the XRD pattern. The peaks were fitted using a Gaussian distribution, and the FWHWM was calculated. The size of the crystal was estimated using the Scherrer equation.

$$B(2\theta) = \frac{K\lambda}{Lcos\theta}$$
[11]

Where B is the FWHWM, K is the shape factor which and for simplicity assumed as 1, L is the crystallite size and θ is the peak angle in radians.

The crystallite size steadily decreases as the Br content is because of a shrinking of the crystal lattice due to increasing concentration of the Br^{-} ion. The bandgap increases with increasing Br

but because of the likely mixed $CsPbBr_3$ phase it is much higher than what is reported in literature [3]. The insets show the color of the film also changed from black to red as the Br content was increased. This change in color indicates a phase shift as the composition becomes Br-rich [12].

5.4 SEM and AFM Analysis
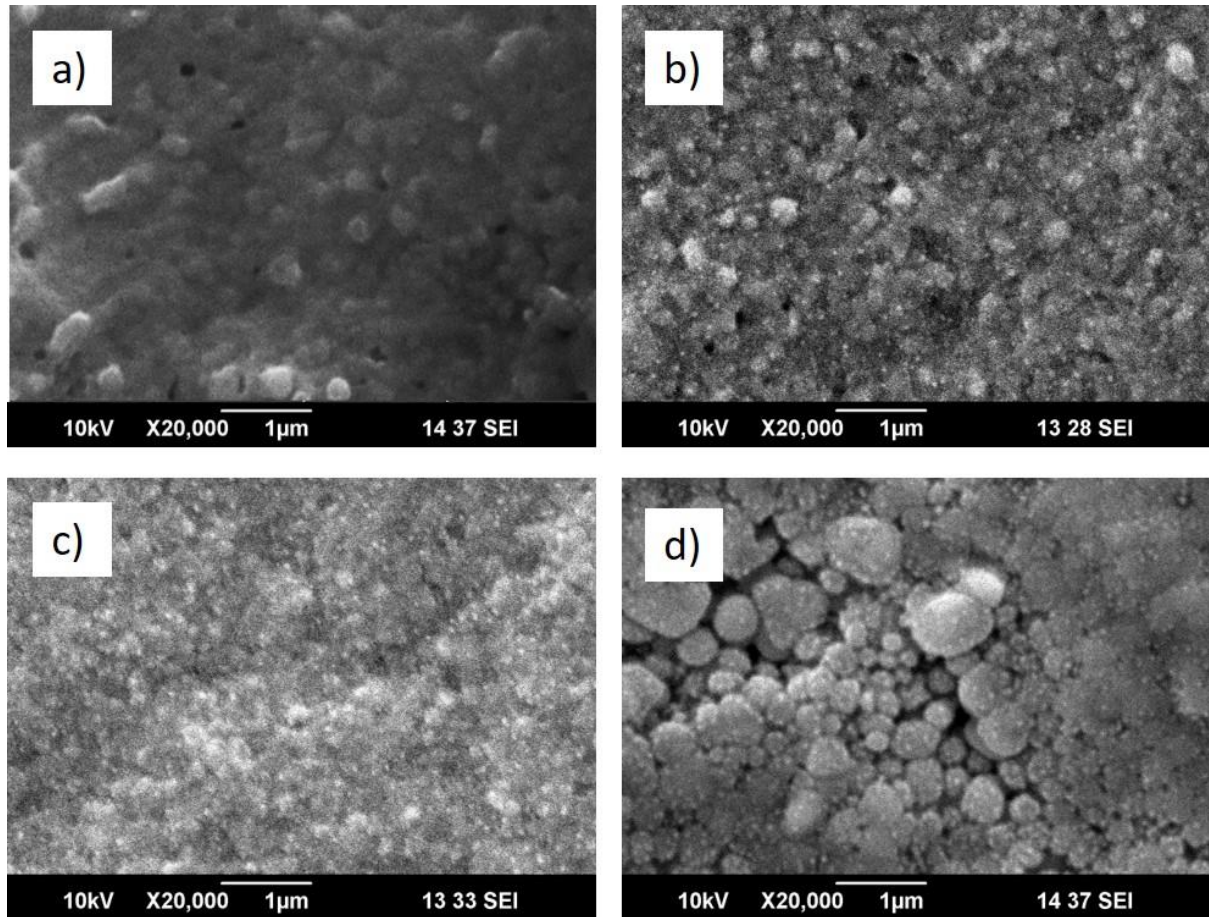
Figure 21: SEM images for (a) $FA_{0.8}Cs_{0.2}PbI_{2.5}Br_{0.5}$ (b)$FA_{0.8}Cs_{0.2}PbI_{2.3}Br_{0.7}$ (c) $FA_{0.8}Cs_{0.2}PbI_2Br$ (d) $FA_{0.8}Cs_{0.2}PbI_2Br$ on glass substrate

The SEM images in Fig. 21 are for four different film compositions. The Br-0.15 film shows small grains with few voids visible in the film. When the concentration of Br is increased to Br-0.5, the film shows more voids in between the grains which show uneven coverage. For the Br-0.7 the grains become non-existent and the film has a very rough appearance. The coverage has somewhat improved but there is no crystalline order which was confirmed by the presence of multiple phases in our XRD pattern. For the Br-1 sample there are larger grains visible in the image. The average grain size was estimated to be 500 nm. These bubble-like grains have agglomerated together however, there are still some voids visible in the film.
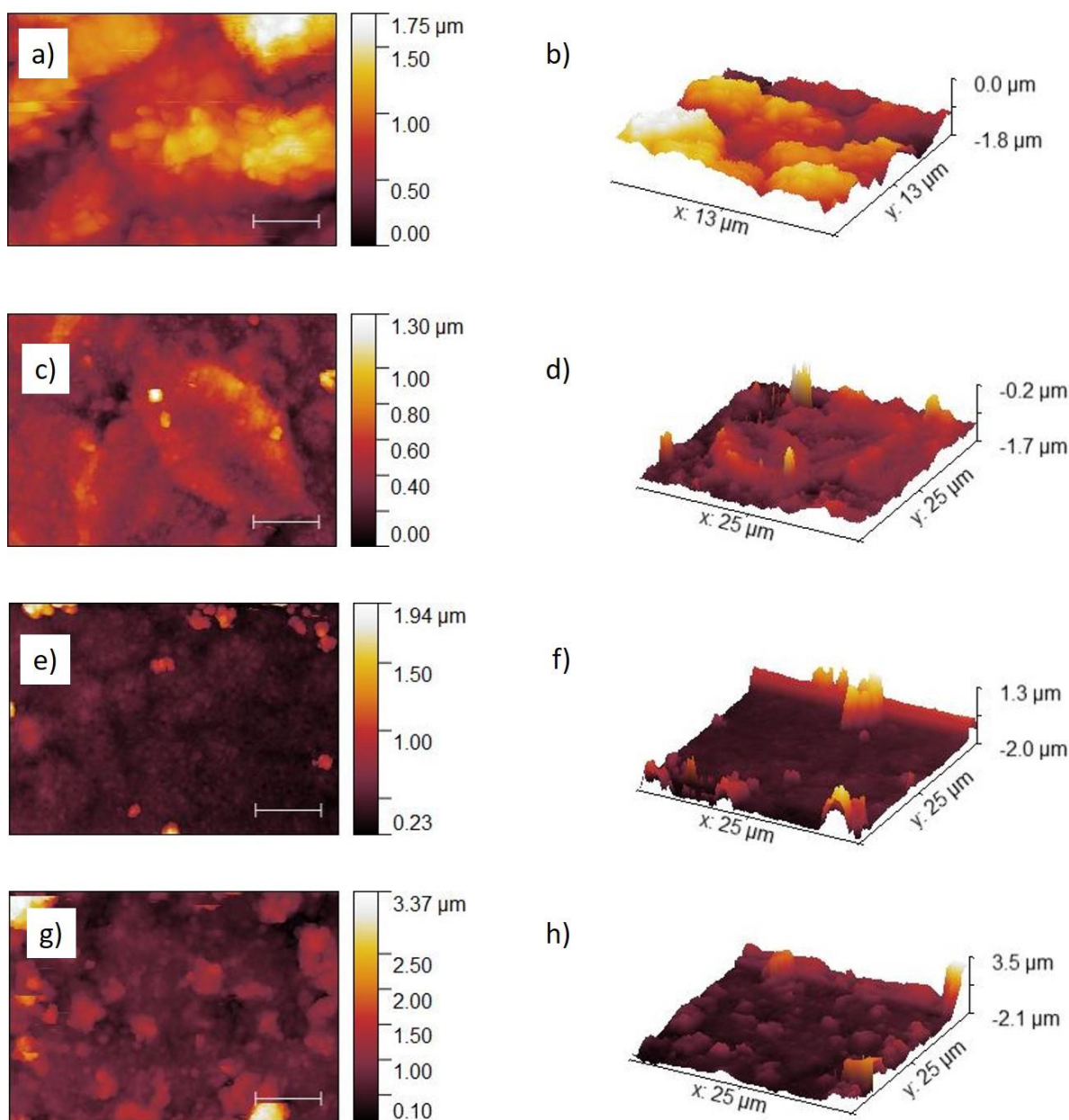
Figure 22: AFM images for (a) FA$_{0.8}$Cs$_{0.2}$PbI$_{2.5}$Br$_{0.5}$ (b)FA$_{0.8}$Cs$_{0.2}$PbI$_{2.3}$Br$_{0.7}$ (c) FA$_{0.8}$Cs$_{0.2}$PbI$_2$Br

To investigate the roughness of the films and get an accurate idea of the grain size distribution of the film, the samples were characterized using AFM. The Br-0.15 sample has an average grain size 92.9 nm which was calculated by edge detection. The Br-0.5 sample the value increased to 148.7 nm. The average roughness of the film was 110 nm. For the Br-0.7 perovskite layer saw a decrease in the grain size to 118 nm which can be explained by a decrease in the crystallite size and is in good agreement with the SEM results. When the Br content was increased to Br-1, the average grain size also increased to 348 nm.

The average roughness of the film for Br-0.15 was 68.7 nm and it increased to 110 nm for the Br-0.5 sample. Further increasing the Br content increased the roughness from 153 nm for Br-

0.7 to 234 nm for Br-1 as it is evident by the non-homogenous topography. The AFM images show that the grain size increases by increasing the Br content of the film, and the roughness also varies in the same way. A rougher absorber layer helps trap more light and reduces reflectance losses [13], but due to the presence of voids it may also impact the device performance.

Summary

The effect of dipping time on the absorbance of the perovskite layer was studied using UV-Vis spectroscopy. Increasing the time, the substrates were immersed lead to a complete conversion of the lead iodide film and improved the light absorbance. A dipping time of 15 minutes was selected and followed for the remaining samples. The XRD analysis showed that the crystallinity of the perovskite improved as the Br content was increased for the $FA_{0.8}Cs_{0.2}PbI_{3-x}Br_x$ film. There was also a presence of a $CsPbBr_3$ phase detected for samples 0.5 and 0.7. The peak analysis showed that the peak around 28° shifted to a higher 2θ value as the Br was increased. This is due to a shrinking of the crystal lattice as more of the smaller Br ion is incorporated into the crystal structure. Similarly, the crystallite size also decreases but the decrease is not linear. The absorbance curves also blue shift and absorption increased in the UV-range with an increase in the Br content, but they do not follow the predicted trend. The calculated bandgap for samples 0.5 and 0.7 is greater than 2 eV which matches with $CsPbBr_3$. This along with the XRD pattern confirms that the Pb prefers the Br ion over the I ion since their bond has a higher complexation constant. The SEM and AFM images show an increase in roughness and the presence of voids in the film.

References

[1] S. A. Kulkarni, T. Baikie, P. P. Boix, N. Yantara, and N. Mathews, "Band-gap tuning of lead halide perovskites using a sequential," 2014.

[2] D. P. McMeekin *et al.*, "A mixed-cation lead mixed-halide perovskite: The ideal absorber for tandem solar cells," *Science (80-.).*, vol. 351, no. 6269, p. accepted, 2016.

[3] "Artifacts in Absorption Measurements of Organometal Halide Perovskite Materials: What Are the Real Spectra?," pp. 3–7, 2015.

[4] L. Atourki *et al.*, "Role of the chemical substitution on the structural and luminescence properties of the mixed halide perovskite thin MAPbI 3-X Br x (0 ≤ x ≤ 1) films," *Appl. Surf. Sci.*, vol. 371, pp. 112–117, 2016.

[5] A. Pengpad *et al.*, "Surface composition of MAPb(I x Br 1−x) 3 (0 ≤ x ≤ 1) organic-inorganic mixed-halide perovskites," *Appl. Surf. Sci.*, vol. 479, pp. 311–317, Jun. 2019.

[6] C. Bi *et al.*, "Understanding the formation and evolution of interdiffusion grown organolead halide perovskite thin films by thermal annealing," *J. Mater. Chem. A*, vol. 2, no. 43, pp. 18508–18514, Nov. 2014.

[7] G. E. Eperon, S. D. Stranks, C. Menelaou, M. B. Johnston, L. M. Herz, and H. J. Snaith, "Formamidinium lead trihalide: A broadly tunable perovskite for efficient planar heterojunction solar cells," *Energy Environ. Sci.*, vol. 7, no. 3, pp. 982–988, 2014.

[8] C. H. Ng *et al.*, "Tunable Open Circuit Voltage by Engineering Inorganic Cesium Lead Bromide/Iodide Perovskite Solar Cells," *Sci. Rep.*, vol. 8, no. 1, pp. 1–9, 2018.

[9] S. Joon Yoon, M. Kuno, and P. V Kamat, "Shif t Happens. How Halide Ion Defects Influence Photoinduced Segregation in Mixed Halide Perovskites," vol. 18, p. 40, 2020.

[10] S. J. Yoon, K. G. Stamplecoskie, and P. V. Kamat, "How Lead Halide Complex Chemistry Dictates the Composition of Mixed Halide Perovskites," *J. Phys. Chem. Lett.*, vol. 7, no. 7, pp. 1368–1373, Apr. 2016.

[11] A. L. Patterson, "The scherrer formula for X-ray particle size determination," *Phys. Rev.*, vol. 56, no. 10, pp. 978–982, Nov. 1939.

[12] G. E. Eperon, S. D. Stranks, C. Menelaou, M. B. Johnston, L. M. Herz, and H. J. Snaith, "Formamidinium lead trihalide: A broadly tunable perovskite for efficient planar

heterojunction solar cells," *Energy Environ. Sci.*, vol. 7, no. 3, pp. 982–988, Mar. 2014.

[13]   V. A. Online, "Improved light absorption and charge transport for perovskite solar cells with rough interfaces by sequential deposition †," pp. 8171–8176, 2014.

Chapter 6: Conclusion and Future Recommendations

6.1 Conclusion

In this work, we studied the optical, morphological, and structural properties of mixed cation and mixed halide wide bandgap perovskite absorber layers fabricated through sequential deposition. The dipping time was increased from 60 s to 15 mins after observing an increase in absorbance. The composition was tuned by keeping the FA and Cs ratio constant while varying the Br and I ratio. The concentration of Br in $FA_{0.8}Cs_{0.2}PbI_{3-x}Br_x$ was increased from 0 to 1.

The structural properties showed that the samples had a perovskite crystal phase and the crystallinity of the layer improved as the Br concentration was increased. This was evident by the sharper peaks at the angles corresponding to a perovskite crystal lattice. The XRD pattern also matched peaks with a $CsPbBr_3$ perovskite for samples with 0.5, 0.7 and 1 molar ratios of Br. This is attributed to the fact that the Br- ion is favored over the I- ion in lead halide perovskites. The structure was further analyzed, and a monotonic shift was observed for the perovskite peak at 28°. The shift to a higher angle showed that the crystal lattice has contracted due to the increase in Br concentration because it has a smaller ionic radius than I^-. This was confirmed by the FWHWM and crystal size calculation and a decrease in crystallite size was observed when the Br concentration was increased. The crystal lattice of the perovskite retained its stability even after the crystal size decreased.

The optical properties of the samples showed the absorbance blue-shifted when the Br concentration was increased however, the shift was non-linear due to the mixed-phase. Overall, the absorbance increased in the ultraviolet range which is ideal for wide bandgap top cells. The bandgap increased from 1.52 eV for the $FAPbI_3$ film to 1.83 eV for $FA_{0.8}Cs_{0.2}PbI_{2.7}Br_{0.3}$ although further increase shifted the absorption onset drastically and the bandgap for samples $FA_{0.8}Cs_{0.2}PbI_{2.5}Br_{0.5}$ and $FA_{0.8}Cs_{0.2}PbI_{2.3}Br_{0.7}$ was in the region of <2 eV which corresponds to that of $CsPbBr_3$. This confirms the presence of a $CsPbBr_3$ phase in the XRD pattern and implies that the I- ion is not incorporating itself into the perovskite crystal structure.

The morphology of the film showed very rough films with the presence of voids. The grain size did increase as the Br concentration was increased. The roughness of the films can be attributed to the sequential deposition process which produces highly disordered layers. The

average grain size estimated from the SEM images for the Br-1 sample was 500 nm which is unusually large for a perovskite absorber layer.

A more accurate calculation of the grain size was carried out using the AFM images. The grain size increased gradually from 148.7 nm to 348 nm. However, not all samples followed this trend and the Br-0.7 appeared to behave as an anomaly with non-existent grains in the SEM image and a smaller calculated grain size of 118 nm. As predicted, the roughness for these films was very high and increased from 110 nm to 253 nm as the Br concentration was increased.

A sequential deposition process leads to a structurally stable absorber layer with increased crystallinity and more ordered smaller lattices as the Br concentration is increased. For a mixed-halide perovskite, it favors the lead bromide perovskite layer because of the higher affinity of Pb towards Br. All the precursors in the dipping solution do not take part in the reaction equally leading to a mixed phase. Increasing the Br concentration widens the bandgap as predicted but the absorbance curves and XRD peaks show it leads to a non-stoichiometric composition with sequential deposition for $x>0.3$ in $FA_{0.8}Cs_{0.2}PbI_{3-x}Br_x$.

6.2 Future Recommendations

1. The number of observations can be increased by preparing more samples with varying compositions of the absorber layer. This will help determine at which exact value of Br does the perovskite layer begin to show anomalous behavior.

2. A more detailed study of the chemical processes involved in the sequential deposition process is required. These can be carried through in-situ measurements of the chemical composition, bond energies and optical properties of the absorber layer.

3. A photoluminescence spectroscopy study can help determine the number of defects present in the film. The recombination losses will give us a better idea on how the film will perform in ambient conditions.

4. A solar cell can be fabricated using these absorber layers to determine their electrical properties. The IV-curve and EQE measurements will let us know whether the light absorbing layer is working as it should be.

5. The deposition process can be modified to address the issues associated with the film. A different solvent can be used in the precursor to compare the results.

Summary

The sequential deposition process gives us structurally stable wide bandgap perovskite absorber layers, but it is difficult to control the stoichiometric ratios for the reaction in the precursor dipping solution. For non-stoichiometric compositions, the Pb ion prefers the Br ion over I ion leading to the formation of a $CsPbBr_3$ phase. This was confirmed in the XRD pattern as well as the absorbance measurements. The films were also very rough and had many voids. It is recommended that more variations of composition and tuning of the bandgap should be performed to determine the point at which the layer begins to show anomalous behavior. In-situ characterization will also help us study the chemical processes involved. The solvent may be changed as a comparison study to see if the film quality improves. By fabricating a cell using these absorber layers we can study the electrical properties which would provide us with more useful information.

Chapter 7: Research Project at ASU

As part of the Energy Materials Lab headed by Dr. Zachary Holman, I had the chance to work on their new joint collaboration with NREL to develop a solar thermophotovoltaic cell. This is a device that uses thermal radiation from a localized heat source and converts it into electricity through a two-step procedure. First, heat from the source is absorbed and remitted as thermal radiation from the selective emitter's surface, then a photovoltaic diode absorbs the the high-energy photons and converts them into electron-hole pairs, which make up the current [1]. This thermophotovoltaic (TPV) cell has three main components:

(i)   a thermal radiative source which heats up the emitter

(ii)   an emitter that has spectral control and photon recycling capabilities

(iii)   a photovoltaic converter

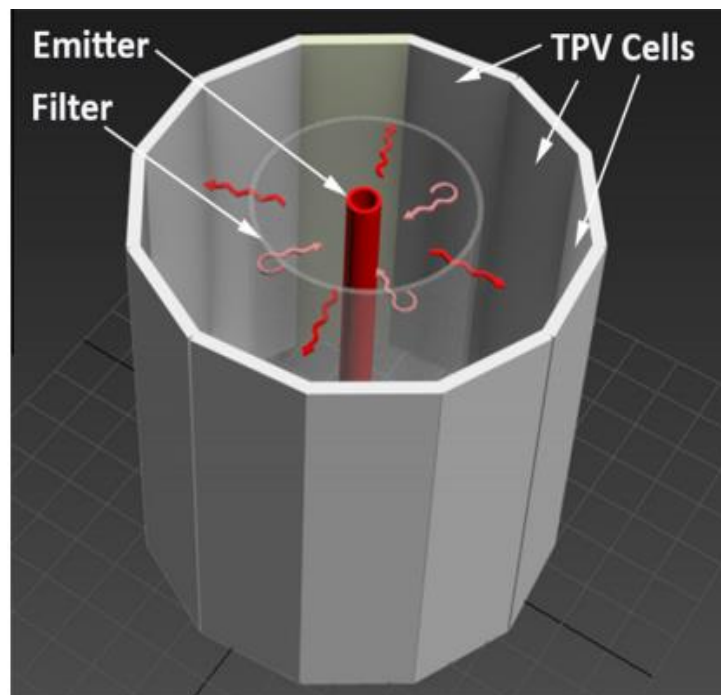*Figure 23: Cross-sectional view of a TPV device*

7.1 Background

Ideally the TPV system should have a high spectral efficiency which can be achieved by matching the emitter's radiative spectrum with the selected photocell's optical sensitivity. The "selective emitter" is made of a material with a narrower thermal radiation range at equilibrium than that of a blackbody at the same temperature.

Since ideal emitters are a limited resource we can use selective filters to recycle the unabsorbed radiation and reflect it back to the emitter. The emitter absorbs the sub-bandgap photons and radiates them with the ideal energy, increasing the overall efficiency. The source of heat can act as a spectral filter itself if it offers low emissivity for a specific photon energy range. In this case, we match emissivity and absorptivity spectrums for the photovoltaic cell [2].

7.1.1 Silicon TPV

Silicon has a bandgap of around 1.1 eV which is an appropriate value for TPV systems if we combine the photocells selective emitters designed to match the emitter's radiation spectrum. Si photocells offers many advantages over other similar materials because of their low cost, abundant nature and non-toxic properties Durisch et al manufactured a TPV system using Silicon cells and Yb_2O_3 thermal emitter to achieve 4% efficiency [3].

7.1.2 GaSb TPV

GaSb is another low bandgap material with a value of of 0.72 eV but it can function in high irradiation density environments, so it is an optimal choice for TPV systems. However, they come with some drawbacks like high costs and toxicity levels. Tang et al. used a simulation tool to model a GaSb thermophotovoltaic cell using a novel p-type doping technique and demonstrated 3.9% efficiency [4].

7.1.3 CIGS TPV

CIGS has a tunable bandgap between 1.0 eV (no Ga) and 1.7 eV by varying the Ga content. CIGS is a popular choice for concentrator solar cells and have achieve efficiencies beyond 20%. Even though the CIGS are toxic in nature, researchers rationalize that using a thin layer sandwiched by other films and sealing it through encapsulation can allow safe usage of the material. Calculations by Bitnar et al (2010) with a CIGS cell of 18.8% efficiency resulted in 2.3–2.5% system efficiencies when used in conjunction with an SnO2 filter [5].

7.1.4 Germanium TPV

Germanium also has a low bandgap of 0.66 eV that is useful for TPV applications as long as the emitter temperature is lower than 1800 K. However, the downside of Ge is that they exhibit lower efficiencies as compared to Si and GaSb. Ge cells are expensive compared to Si but still an affordable alternate to GaSb and other low bandgap III-V materials. Fraunhofer used a Germanium TPV cell with a Er2O3 selective emitter to achieve a 5.34% efficiency [3].

7.1.5 III-V Materials

We can achieve considerable efficiencies using III-V materials and match ones shown by GaSb cells. These compounds also allow us to reach very low bandgaps and fabricate cells ideal for thermophotovoltaic applications. There are additional developments required to make fabrication cost-effective. Some examples of III-V materials used as solar TPV cells are InGaAsSb, InAsSb, AlGaAsSb, InGaSb, InGaAs and InAsSbP. 0.55 eV bandgap InGaAs exhibited a total power efficiency of 7.6% under 1500°C as demonstrated by Wojtczuk [6].

7.2 Objectives

A thermophotovoltaic device is made up of many components each with their own efficiencies which combined together makeup the overall system efficiency. The limited output of the heat energy to radiation, spectral range limitations and low photovoltaic conversion rates are the biggest loss contributors for TPV systems. Due to the novel nature of the project, an extensive review of the literature was required.

- Survey literature for previous solar thermophotovoltaic cells and their efficiencies
- Characterize III-V solar cells to measure the reflectance of each layer
- Model the cell using SunSolve to identify sources of reflectance losses
- Identify suitable anti-reflective coating materials and simulate cells with reduced losses

7.3 Outcomes
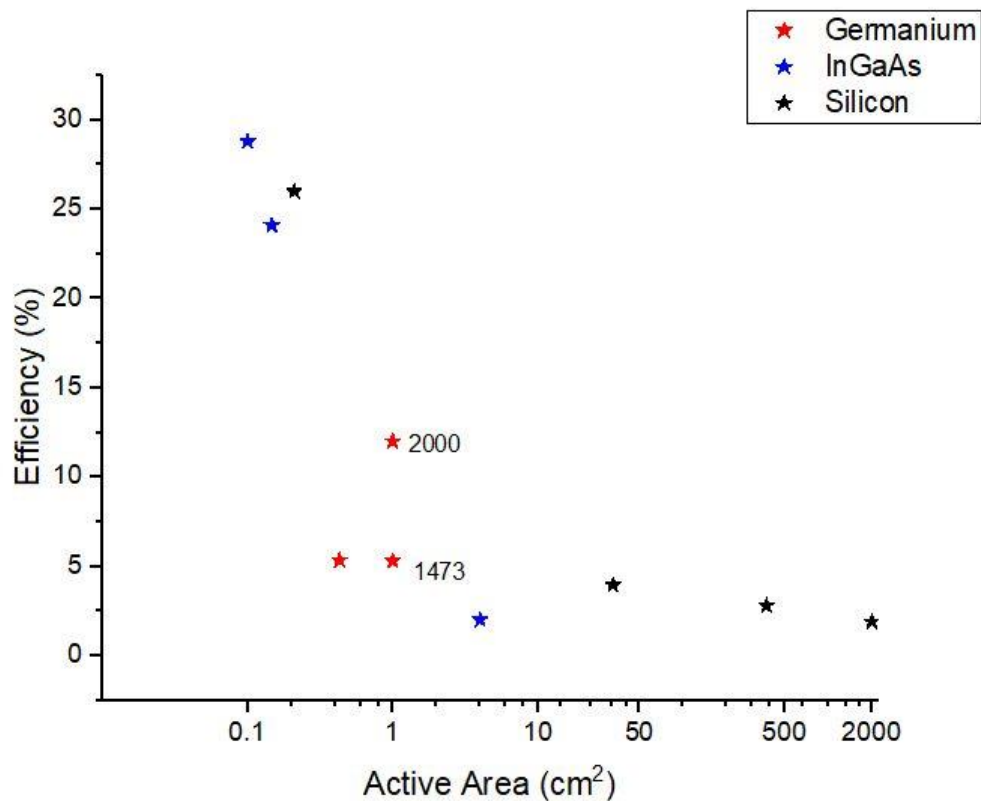
Figure 24: Summary of TPV efficiencies vs. active area of the cell [3,7–13]

There have been some reports in the literature of thermophotovoltaic cells and a summary of their results was compiled in the figure above. The most commonly used materials for the TPV cell were silicon, germanium, and the III-V material InGaAs. The active area of the cell is the key characteristic controlling the efficiency and a large area translates into a lower efficiency. There is the prospect of improving the efficiency of large area TPV solar cells as it is evident in the large empty area of the graph.

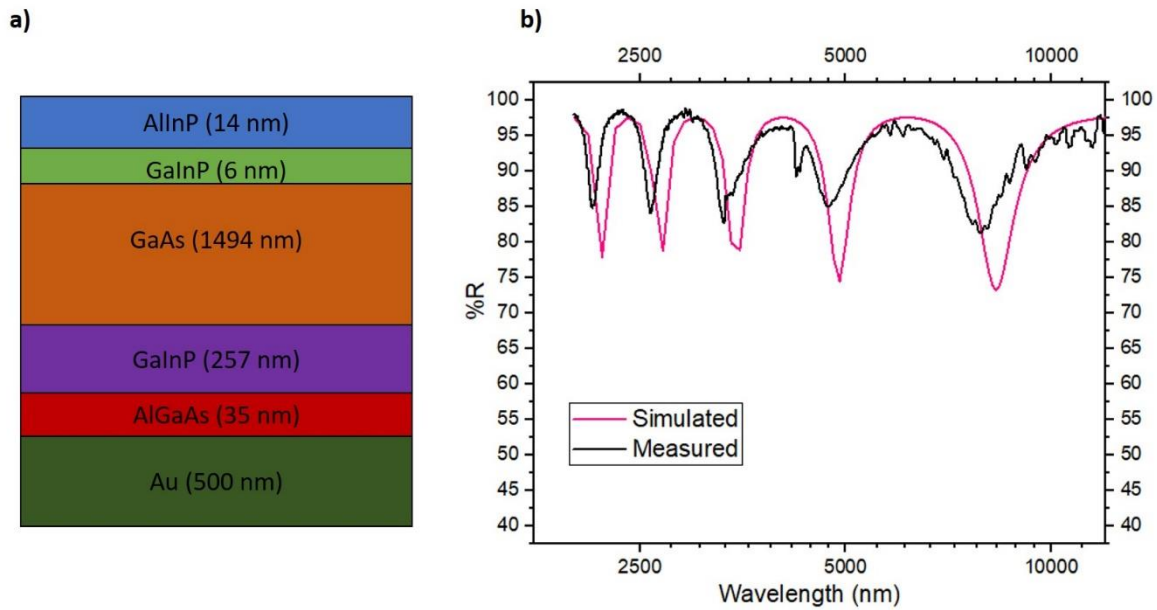*Figure 25 (a): cross-sectional view of TPV cell, (b) Comparison of simulated and measured total reflectance data*

NREL fabricated sample solar cells with a GaAs active layer to measure the reflectance losses. The spectral reflectance of the cells was measured using FTIR. The cells were then modelled using SunSolve and the optical constants for each layer to compare the actual cell's performance with the simulated cells. The simulated data is in good agreement with the measured data with the exception of a few fringes which might be due to the ellipsometry curve fitting errors. The actual cells are affected by many environmental factors which the simulations do not take into account, hence they had a noisier reflectance response.
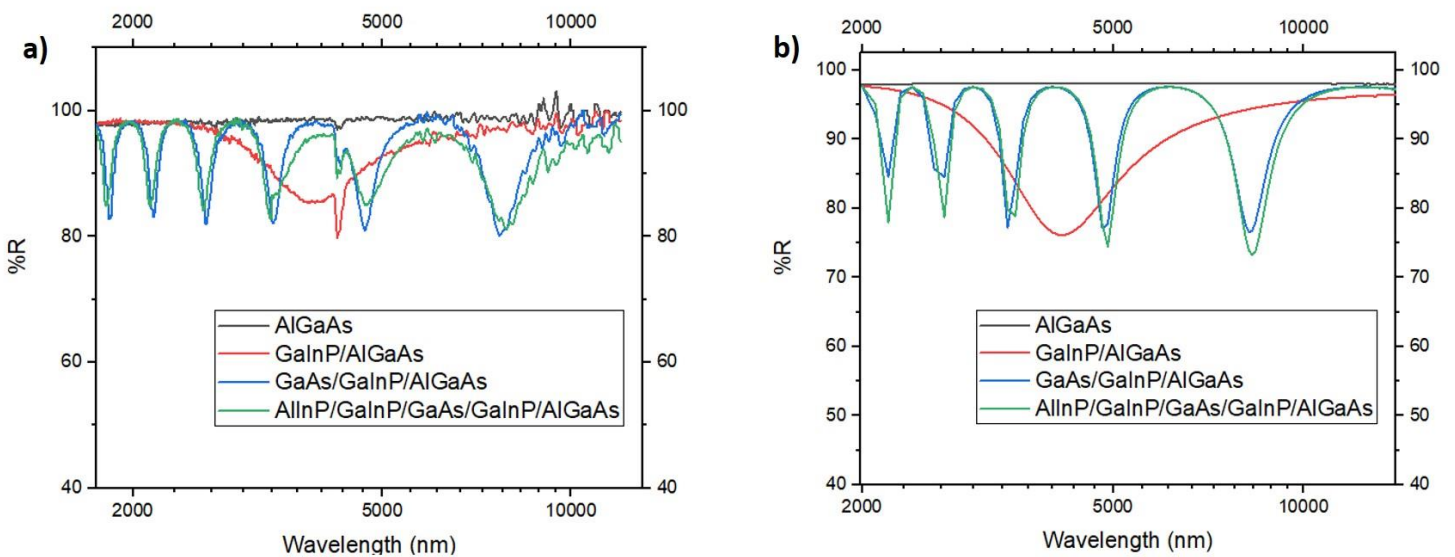
Figure 26 (a): Measured reflectance of each layer of the cell, (b) simulated reflectance using SunSolve

Table 5: Summary of measured and simulated reflectance loss within each layer

Layer	Measured Loss	Simulated Loss
GaInP BSF	1.26%	1.26%
GaAs	2.8%	2.72%
GaInP	3.57%	3.57%
AlInP		

The reflectace of each layer was measured by etching off the subsequent film in order to identify source of optical losses. The simulated and measured data followed a similar trend and the percentage losses were almost identical. The GaInP back surface field accounted for 1.26% of the reflectance loss, while the GaAs absorber layer lowered the reflectance by 2.8%. The majority of the losses were due to the GaInP and AlInP layers which collectively resulted in a 3.57% loss.

Table 6: Characteristics of possible materials for an antireflective coating

| Material	n	k	%R	%T	A	Spectral Range	Deposition	Thickness	Substrate	Application
Polyvinylidene Fluoride	1.42		4%	95%	1% at 3 μm	1 to 7 μm	laser irradiation	25 μm		Micro lenses
BaF_2	1.3	2.25×10^{-5}	5%	94%	1% at 6 μm	1 to 11 μm	ebeam evaporation	6.3 μm	ZnSe	CO2 laser
CaF_2	1.43	3.4×10^{-6}	5%	94%	0.03% at 2.7 μm	3.5 to 10.5 μm	ion-assisted laser deposition	1 mm	GaAs	IR transmitting filter
LaF_3	1.51	0.054	10%	90%	N/A	0.2 to 11 μm	ebeam evaporation	1 mm	CaF2	ArF laser
MgF_2	1.41	0.014 at 2μm	2%	95%	3.3% at 2.7 μm	0.12 to 7 μm	ion-assisted laser deposition	1 mm	glass	CO2 laser
NaF	1.32	2.3 at 9 μm	1%	96%	3% at 7 μm	0.14 to 11 μm	Mo boat evaporation	2 mm	CsI	Photocathode
PbF_2	1.78	0.01	13%	83%	3.7% at 4 μm	0.25 to 11 μm	ebeam evaporation	10 mm	ZnSe	DF laser
SrF_2	1.44	0.01	2%	95%	3% at 5 μm	0.15 to 11 μm	ebeam evaporation	1 mm	Silica	IR ARC
SiO_2 (porous)	1.23		0.60%	99.40%	0.01% at 1 μm	7 to 25 μm	PECVD	132 nm	glass	Si solar cells
Ta_2O_5	2	0.001	3%	96%	0.02 at 10 μm	2.5 to 5.6 μm	reactive magnetron sputtering	50nm	Si	AR on solar cells
AlF_3	1.31	0.001			1% at 8 μm	0 to 11 μm	ebeam evaporation	1480 nm	Ge, ZnSe	Laser
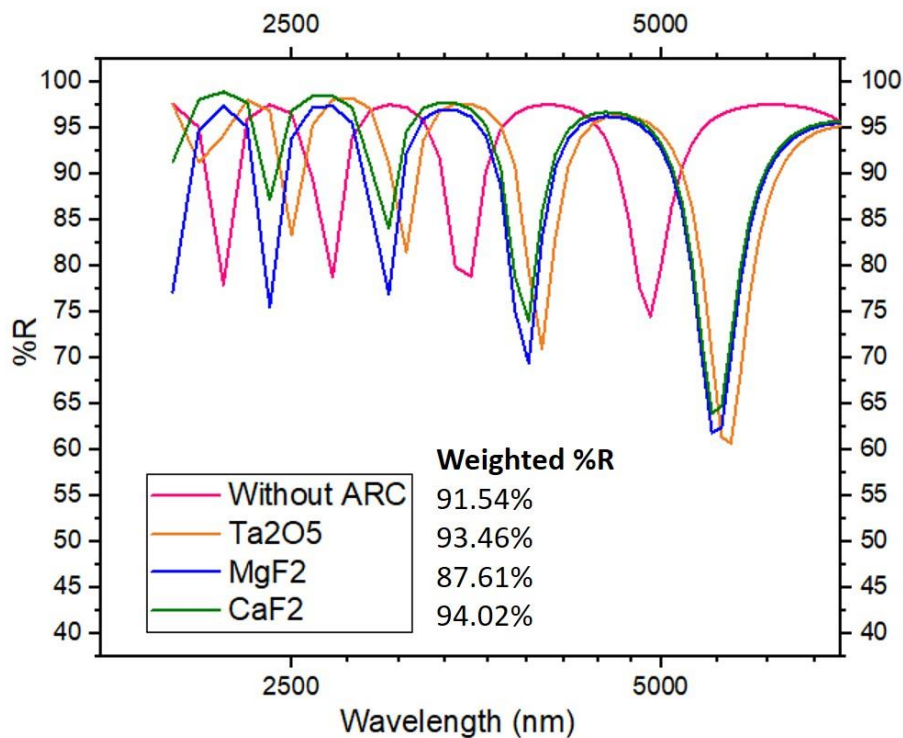
Figure 27: TPV cell reflectance with antireflective coating

The literature reported many promising options for an antireflective coating especially in the category of fluoride dielectrics. BaF_2 and NaF showed exceptional antireflective properties but were not viable for thermophotovoltaics due to their water-soluble nature. CaF_2, MgF_2 and Ta_2O_5 emerged as possible candidates. An antireflective layer was added between the gold contacts and the back surface field using SunSolve. The obtained reflectance results show that an antireflective layer will help transmit more light into the cell. CaF_2 improved the overall reflectance to 94.02% while Ta_2O_5 brought it up to 93.46%

7.4 Conclusions and Future Recommendations

Antireflective coatings offer a suitable amount of reflectance recovery and can help bring up the overall reflectance of the TPV by almost 3%. There is a lot more work to be done in the project to reduce the absorption losses and get reflectance up to 98%.

1. A dielectric anti-reflection coating will be added to the cell structure to measure the reflectance and test the compatibility

2. Possible texturing on the surface of the coating to allow useful light transmiton into the cell

3. The measuring of the J-V characteristics of the curve to see if it behaves as predicted

References

[1] Daneshvar H, Prinja R, Kherani NP. Thermophotovoltaics: Fundamentals, challenges and prospects. Appl Energy 2015;159:560–75. https://doi.org/10.1016/j.apenergy.2015.08.064.

[2] Ganapati V, Xiao TP, Yablonovitch E. Ultra-Efficient Thermophotovoltaics Exploiting Spectral Filtering by the Photovoltaic Band-Edge 2016:1–14.

[3] Bitnar B, Durisch W, Holzner R. Thermophotovoltaics on the move to applications. Appl Energy 2013;105:430–8. https://doi.org/10.1016/j.apenergy.2012.12.067.

[4] Tang L, Ye H. A Novel Zinc Diffusion Process for Fabrication of High Performance GaSb Thermophotovoltaic Cells. In: Oral AY, Bahsi ZB, Ozer M, editors. Int. Congr. Energy Effic. Energy Relat. Mater., Cham: Springer International Publishing; 2014, p. 191–8.

[5] Durisch W, Bitnar B. Novel thin film thermophotovoltaic system. Sol Energy Mater Sol Cells 2010;94:960–5. https://doi.org/10.1016/J.SOLMAT.2010.01.024.

[6] Wojtczuk S. Low bandgap InGaAs thermophotovoltaic cells. IECEC 96. Proc. 31st Intersoc. Energy Convers. Eng. Conf., vol. 2, IEEE; n.d., p. 974–8. https://doi.org/10.1109/IECEC.1996.553831.

[7] Omair Z, Scranton G, Pazos-Out'on LM, Xiao TP, Steiner MA, Peterson PF, et al. Pushing the Limits of Thermophotovoltaic Efficiency. 2018 IEEE 7th World Conf. Photovolt. Energy Convers. (A Jt. Conf. 45th IEEE PVSC, 28th PVSEC 34th EU PVSEC), IEEE; 2018, p. 3685–7. https://doi.org/10.1109/PVSC.2018.8547282.

[8] Woolf DN, Kadlec EA, Bethke D, Grine AD, Nogan JJ, Cederberg JG, et al. High-efficiency thermophotovoltaic energy conversion enabled by a metamaterial selective emitter. Optica 2018;5:213. https://doi.org/10.1364/OPTICA.5.000213.

[9] Swanson RM. Silicon photovoltaic cells in thermophotovoltaic energy conversion. 1978 Int. Electron Devices Meet., IRE; 1978, p. 70–3. https://doi.org/10.1109/IEDM.1978.189354.

[10] Khvostikov VP, Khvostikova OA, Gazaryan PY, Sorokina SV, Potapovich NS, Malevskaya AV, et al. Photoconverters for Solar TPV Systems. 2006 IEEE 4th World Conf. Photovolt. Energy Conf., IEEE; 2006, p. 667–70.

https://doi.org/10.1109/WCPEC.2006.279543.

[11] van der Heide J, Posthuma NE, Flamand G, Geens W, Poortmans J. Cost-efficient thermophotovoltaic cells based on germanium substrates. Sol Energy Mater Sol Cells 2009;93:1810–6. https://doi.org/10.1016/j.solmat.2009.06.017.

[12] Khvostikov VP, Khostikov OA, Oliva EV, Rumyantsev VD, Shvarts MZ, Tabarov TS, et al. Zinc-diffused InAsSbP/InAs and Ge TPV cells. Conf. Rec. Twenty-Ninth IEEE Photovolt. Spec. Conf. 2002., IEEE; n.d., p. 943–6. https://doi.org/10.1109/PVSC.2002.1190736.

[13] Durisch W, Bitnar B, von Roth F, Palfinger G. Small thermophotovoltaic prototype systems. Sol Energy 2003;75:11–5. https://doi.org/10.1016/S0038-092X(03)00232-9.

Appendix: Journal Article

Investigating the Sequential Deposition Route for Mixed Cation Mixed Halide Wide Bandgap Perovskite Absorber Layer

Muneeza Ahmad[a], Nadia Shahzad[a*], Muhammad Ali Tariq[a], Abdul Sattar[a]

[a]*U.S.-Pakistan Center for Advanced Studies in Energy*

National University of Sciences and Technology, H-12, Islamabad 44000, Pakistan

* Corresponding author (email ID: nadia@uspcase.nust.edu.pk)

Abstract

Wide bandgap perovskite solar cells are emerging as the preferred choice for top cells in a tandem architecture with crystalline silicon solar cells. This is due to their bandgap tunability (1.6 to 3eV), low-temperature solution processing, fast charge carrier rate, long carrier diffusion length, and high absorbance in the visible region. Among the wide bandgaps perovskites, a mixed cation, mixed halide composition containing $Cs_xFA_{1-x}PbI_{3-y}Br_y$ is a popular choice because the presence of Br widens the bandgap and the addition of Cs stabilizes the crystal structure. However, these perovskite layers were fabricated using a one-step spin-coating technique even though sequential deposition offers more control over the crystallization process. In this paper, we have fabricated a $Cs_{0.2}FA_{0.8}PbI_{3-x}Br_x$ perovskite absorber layer using sequential deposition. The concentration of Br was varied from 0 to 1, and the optical, structural and morphological properties of the film were studied. As the concentration of Br was increased, the perovskite showed better crystallinity with the presence

of another perovskite phase matching CsPbBr$_3$ detected beyond Br-0.3 owing to a preference for the Pb-Br over the Pb-I complex. Optically, the perovskite films exhibited a higher absorbance in the ultraviolet range of 300-500 nm. The morphology showed the presence of large grains with high surface roughness. This study explores compositional tuning via the sequential deposition route for a wide bandgap perovskite absorber layer.

Keywords: perovskite, sequential deposition, wide bandgap, absorber layer

1. Introduction

Perovskite materials (ABX$_3$) have emerged as an effective light absorbing layer material for photovoltaic solar cells. They possess attractive properties such as high absorbance over the visible spectrum range, resistance to defect formation, fast carrier transport, and long electron/hole diffusion length [1]. Furthermore, the solutions are processed at low temperatures, the materials are abundantly available, and the material can be chemically tuned, making it a viable option for low-cost, large-scale production of flexible solar cells [2].

All these advantages have led to rapid breakthroughs in the technology, and the power conversion efficiency has increased beyond 25% in the last decade [3–6]. The rapid success has made organic-inorganic lead halides a contender for the commercialized crystalline silicon, amorphous silicon thin film, and CdTe photovoltaic cells [7].

The compositions can be varied to form the perovskite crystal structure as long as the atomic size differences are within the tolerance factor [8]. This property can be used to tune the perovskite material's bandgap over a wide range of wavelengths, from 1.15 to 3 eV, i.e., infrared to ultraviolet [9]. Wide bandgap PSCs with E$_g$ over 1.7 eV is ideal for the top subcell in tandem with both crystalline silicon and low bandgap PSC bottom sub cells [10]. The bandgap can be tuned by substituting the iodide anion with bromide. Increasing the Br- content can result in a wider bandgap for the perovskites [11]. The Cs-FA, mixed cation wide bandgap

perovskite, is also more thermally stable than MAPbI$_3$ [12]. Many researchers have realized the importance of wide bandgap perovskites and dedicated their resources to improve efficiency and stability [13, 14].

McMeekin et al. substituted the formamidinium cation with cesium to eliminate phase instability of the halide domains and achieve a wide bandgap absorber layer [15]. The addition of Cs also widens the bandgap, and they exploited that property to push the Br-to-I unstable phase to a higher energy space. The champion cell displayed a short current density equal to 19.4 mA cm^{-2} with an open-circuit voltage of 1.2 V, and a PCE of 17.1%. .Lin et al. added Cs to the FA-based perovskites because it brings stability to the perovskite film [16]. They recorded a stabilized PCE of 18.5% for their solution-processed wide bandgap perovskite solar cell.

However, both research groups use the one-step deposition technique. It has been suggested that the sequential deposition technique is far superior in terms of crystallization. The deposition technique makes all the difference in its performance. The film coverage, quality of the absorber layer, and its transport properties depend on it [17]. An efficient and stable perovskite layer was deposited using the two-step deposition technique by Gratzel and his team [18]. The sequential process allows better control over the crystallization because the perovskite is divided into two precursor solutions [19].

Xie et al. used a sequential deposition process to fabricate a MAPbI$_3$ solar cell by introducing a small amount of MAI to the PbI$_2$ solution [20]. The additive improved the absorption of the films due to enhanced crystallization and a reduction in carrier recombination rate. Their method introduced a new route for efficient sequential deposition of the MAPbI$_3$ absorber layer. Koh et al. used a sequential deposition technique to fabricate the FAPbI$_3$ perovskite layer

[21]. Another research group Kulkarni et al., utilized the sequential deposition procedure to tune the bandgap of a $MAPb(I_{1-x}Br_x)_3$ perovskite solar cell [22].

To the best of our knowledge, there is no research on FA-based wide bandgap perovskites fabricated using the sequential deposition technique even though it offers better transport properties and film coverage [17]. This research aims to demonstrate whether a sequential deposition is a viable technique for perovskite containing Cs and FA cations. We have explored the optical, structural and morphological properties of a wide range of compositions for a full exhaustive study sequential deposition for wide bandgap deposition. In the absorber layer, PbI_2 was spincoated on FTO substrates and then substrates were dipped into the CsBr, FABr/ FAI solutions with varying ratios, resulting in a homogeneous film with good surface coverage.

2. Experimental Methodology

2.1 Film Deposition

The formamidine acetate salt (CAS No. 3473-63-0), lead iodide salt (CAS No 10101-63-0), cesium bromide salt (CAS No. 7787-69-1), formamidnium bromide salt (CAS No. 146958-06-7) and FTO coated glass (EC No. 242-159-0) were purchased from Sigma Aldrich. The hydroiodic acid was bought from Alfa Aesar (CAS No. 10034-85-2).

The formamidinium iodide was synthesized using a method adapted from the literature with modifications [23]. 2 molar excess of formamidine acetate salt was stirred into 10ml of methanol over an ice bath. 57% w/w hydroiodic acid was added into the flask drop-wise under constant stirring and then left to stir at 0°C for two hours. The solvents were carefully evaporated using a rotary evaporator at 75-80°C for five hours. After evaporation a precipitate

was left behind which was then washed with excess amounts of diethyl ether until it was off-white in colour. The crystals were dried at 60°C in a vacuum oven for 24 hours before use.

The glass and FTO-coated glass slides were kept in a mild detergent solution and then sonicated for 15 minutes. After rinsing with deionized water, the slides were sonicated in isopropyl alcohol, acetone then isopropyl alcohol sequentially for 15 minutes each. They were dried in air and heated on a hot plate at 70 degrees before spincoating.

A 1M solution of PbI_2 was prepared by mixing 461 mg of PbI_2 in 1 ml of DMSO and DMF with a 2:3 ratio. The solution was stirred for 1 hour at 70 degrees and kept at that temperature during the spincoating procedure. The solution was spincoated onto the glass and FTO glass substrates at 2000 rpm for 25 s. The films were dried on a hot plate at 70 °C for 10 mins.

The slides were then shifted to a globebox and dip coated in a solution of CsBr, FAI and FABr in IPA to achieve varying ratios. For example 0.2 mM of CsBr, 0.5 mM of FAI and 0.5 mM of FABr was used for $FA_{0.8}Cs_{0.2}PbI_{2.5}Br_{0.5}$. The composition of Br was kept at 0, 0.3, 0.5, 0.7 and 1.

Initially the PbI_2 films were dipped in the CsBr and FAI solution for only 60 seconds because the literature on sequentially deposited MAPbI3 films suggested longer dipping times can cause poorer film coverage and lead to the formation of shunt pathways in the absorber layer [24]. However, experiments involving Br required a longer dipping time for complete conversion of the perovskite layer [22] so it was increased to 15 mins. This was followed by drying on a hot plate at 120 °C for 30 minutes.

2.2 Characterization

For the structural investigation and crystal size analysis of the perovskite films, the X-ray Diffraction (XRD) technique was used through the Bruker, D8 Advanced with a scanning rate of 1.2/min and 2θ in the range of 5° to 70°. The XRD used a CuKα radiation source (λ=1.54056

Å) generated at an excitation voltage 40 kV and current 40 mA. MDI Jade 6.5 was used for the peak analysis, hkl determination and signal processing.

The surface morphology of the films was captured using the Scanning Electron Microscope (SEM). For the scanning a MIRA3 TESCAN was used. The images were recorded for 10.0 Kx magnification and a voltage of 10.0 KV was set for the scans.

To study the optical properties of the perovskite, the UV-Vis NIR Spectrophotometer UV-3600 Plus was used. The asborbance of the samples was measured in the range of 300 to 1100 nm with a slit width of 2.5 µm.

The surface topography and roughness was investigated using the Atomic Force Microscopy technique. A Nanosurf FlexAFM Version 5 was used in static mode. The feature size was kept at 2.5 µm and the expected height was 1.5 µm. The images were analyzed and processed using the Gwyddion software.

The film thickness was recorded using a 2D Optical Profilometer. It was a non-contact instrument PS-50 from Nanovea. A scanning length of 12 mm was used to measure the average height of the film.

All measurements and characterizations were carried out ex-situ.

3. Results and Discussion

3.1 Dipping Time Effect

The dipping time of the PbI_2 films was varied from 60 seconds to 15 minutes because it was suggested in the literature that perovskite layers involving Br require longer dipping times [22]. According to the UV-Vis spectroscopy results shown in Fig. 1(a), a longer dipping time resulted in a higher absorbance of the film. This can be attributed to complete conversion of the perovskite and increased crystallinity as shown in Fig. 1(b). The film prepared by dipping for 60 secs in the precursor solution shows a strong presence of PbI_2 peaks labelled with an ampersand sign. The suppression of these peaks and the larger perovskite phase peaks point towards a more crystalline perovskite structure with very little residual PbI_2 [25]. The absorbance also increased as the CsBr content in the film is increased since the presence of Cs promotes the crystallization of the film [15]. The absorbance curves observed for these films tend to be flat which could also be due to the larger crystal size and higher thickness of the film [26]. All the following samples were fabricated using a dipping time of 15 minutes.
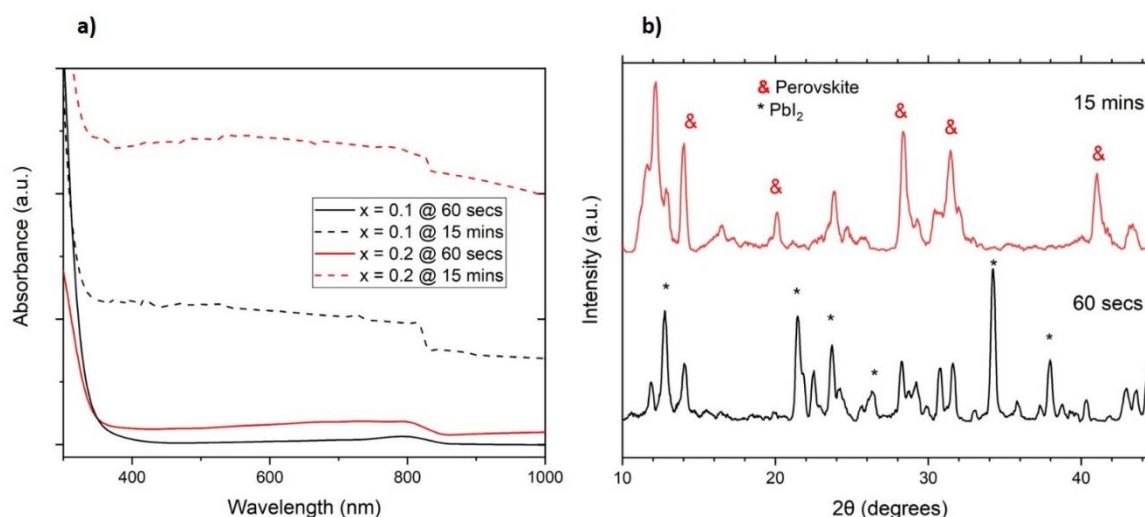

Figure 28(a) Absorbance curves for the $FA_{1-x}Cs_xPbI_{3-x}Br_x$ perovskite layers where x represents the molar ratio of CsBr used.(b) XRD pattern for one sample after increasing dipping time from 60 secs to 15 mins. The red ampersand denotes a perovskite peak and the black asterisk is a label for PbI_2 peaks.
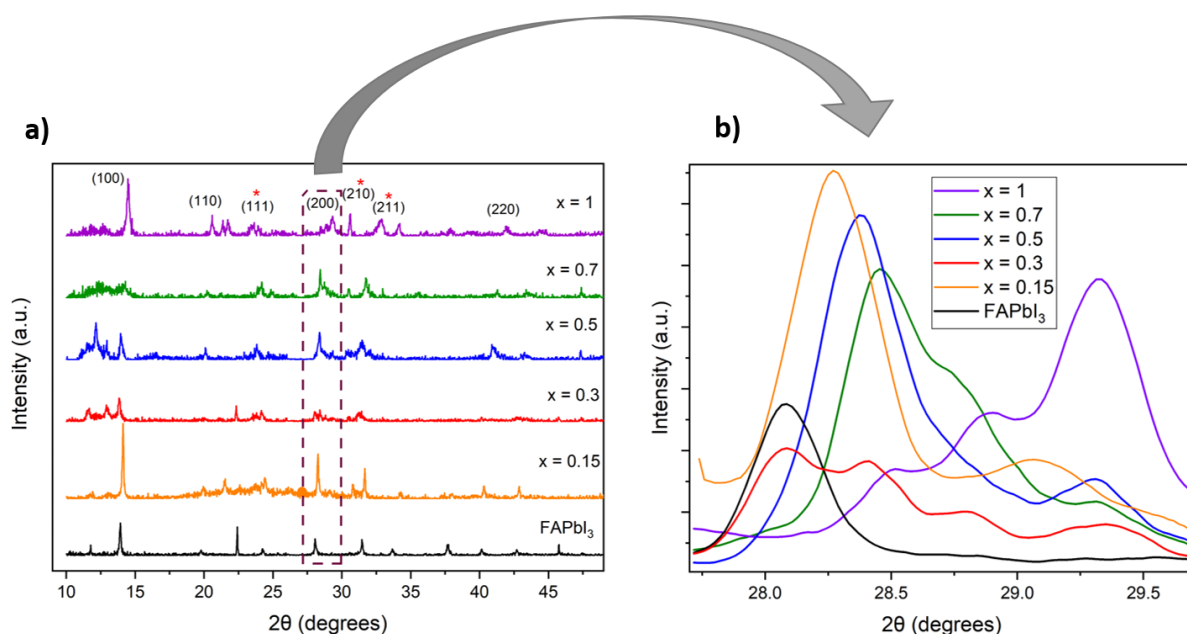
84

3.2 XRD Analysis

Figure 29*(a) XRD pattern for the FAPbI₃ and FA₀.₈Cs₀.₂PbI₃₋ₓBrₓ perovskite layers labelled by the concentration of Br used. The red asterisk corresponds to the CsPbBr₃ peaks.(b) XRD pattern magnified at the 28° peak*

The XRD patterns for the different film compositions are shown in Fig. 2(a). The characteristic perovskite peaks at 14° (100), 20° (110), 28° (200), 40° (220) become more prominent and shift to larger angles as the Br content is gradually increased. However, the PbI_2 peak at 12° remains present throughout the different compositions showing the presence of remnant PbI_2 film. There is also the existence of another prominent phase in the Br 0.5, 0.7, and 1 films, which is visible at 24° (111), 30° (210), and 34° (211). These values match with the $CsPbBr_3$ perovskites, and it seems that only the CsBr is incorporating itself into the lattice while the FAI and FABr are being rejected. The ionic radius of Cs (179 pm) is smaller than that of FA (250 pm), which could be the reason it is easily inserted into the structure.

Fig. 2(b) shows a magnification of the XRD peak around 28°. The signal has been processed, so the relative height of the peak does not depict the actual intensity. However, as it is visible from the graph, the peak shifts to a larger angle as the ratio of Br is increased. The peak observes a monotonic shift from 28.2° for $FAPbI_3$ to 29.6° for Br-1. This is characteristic of shrinkage

of the lattice and a reduction in crystal size. As more and more of Br is added to the ratio, the

I is replaced. Since Br^- has a smaller ionic radius than I^- it causes the lattice to contract. These

claims can be supported by what has already been reported in the literature [27, 28].

Additionally, it is interesting to note that the relative intensity increases as more Br is added to

the precursor, which shows a more ordered and crystalline perovskite phase [29].
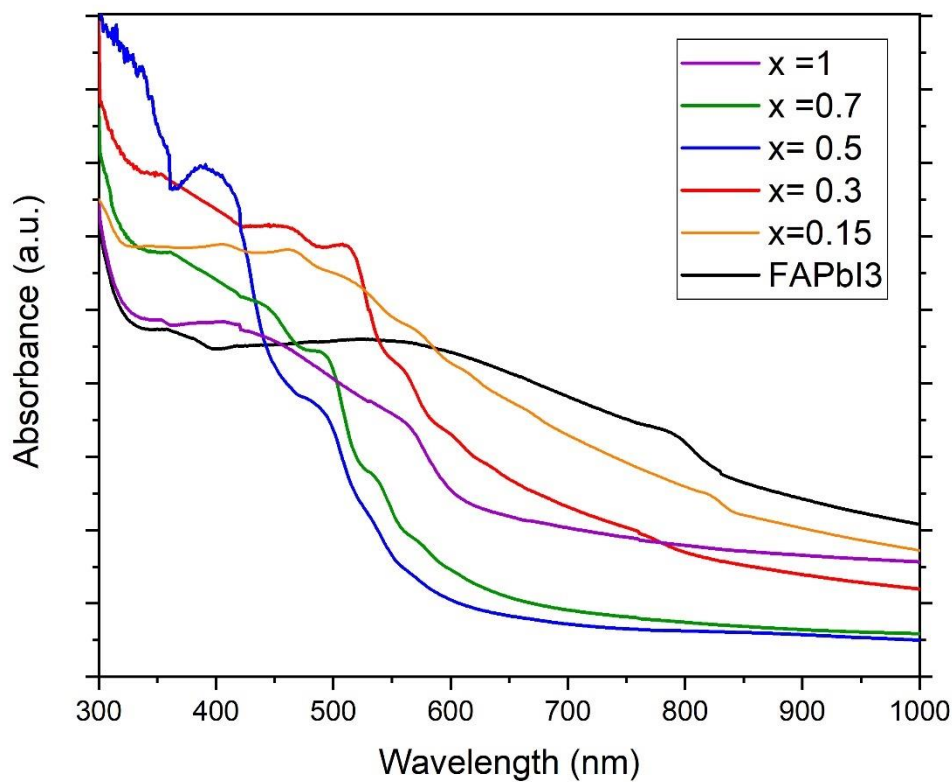
3.3 Optical Properties

Figure 3 *Absorbance curves for the FAPbI$_3$ and FA$_{0.8}$Cs$_{0.2}$PbI$_{3-x}$Br$_x$ perovskite layers*

The absorbance graph for the FAPbI$_3$ sample has an absorption onset around 830 nm which

corresponds to the bandgap of 1.49 eV as reported in the literature [30]. When the bandgap was

calculated through a Tauc plot using the thickness of 5μm obtained from the profilometry, it

was 1.52 eV. The same value was obtained for the Br-0.15 sample. The Br-0.3 absorbance is

blue shifted and has a bandgap of 1.83 eV. However, as the percentage of Br is increased, the

absorbance curves are greatly blue shifted. The bandgap increases to greater than 2eV for Br-

0.5 and Br-0.7. It is closer to a bandgap of CsPbBr$_3$ which has been reported to be 2.3 eV. In the absorbance graph there is a distinct absorption edge around 500 nm which is characteristic of CsPbBr$_3$ [31]. This corroborates the presence of the CsPbBr$_3$ peaks in the XRD pattern and proves that the FA cation is not being included in all the perovskite crystal structure. The CsBr salt proves to be more dominant and the reason for that is the seven-times higher complexation constant between the Pb-Br species [32, 33]. The higher affinity of Pb^{2+} towards Br$^-$ ion leads to the I$^-$ ion playing the role of a spectator. The Br-1 film, however, has a lower bandgap of 2 eV and the absorption onset is also red-shifted because a higher concentration of FABr was used to achieve this composition and therefore FA was included in the perovskite structure. The overall absorbance increased in the ultraviolet range i.e. 300-500 nm which ideal for wide bandgap materials. As inferred in the literature, the sharp increase in absorbance shows that the samples' crystallinity improves by adding more Br [15].
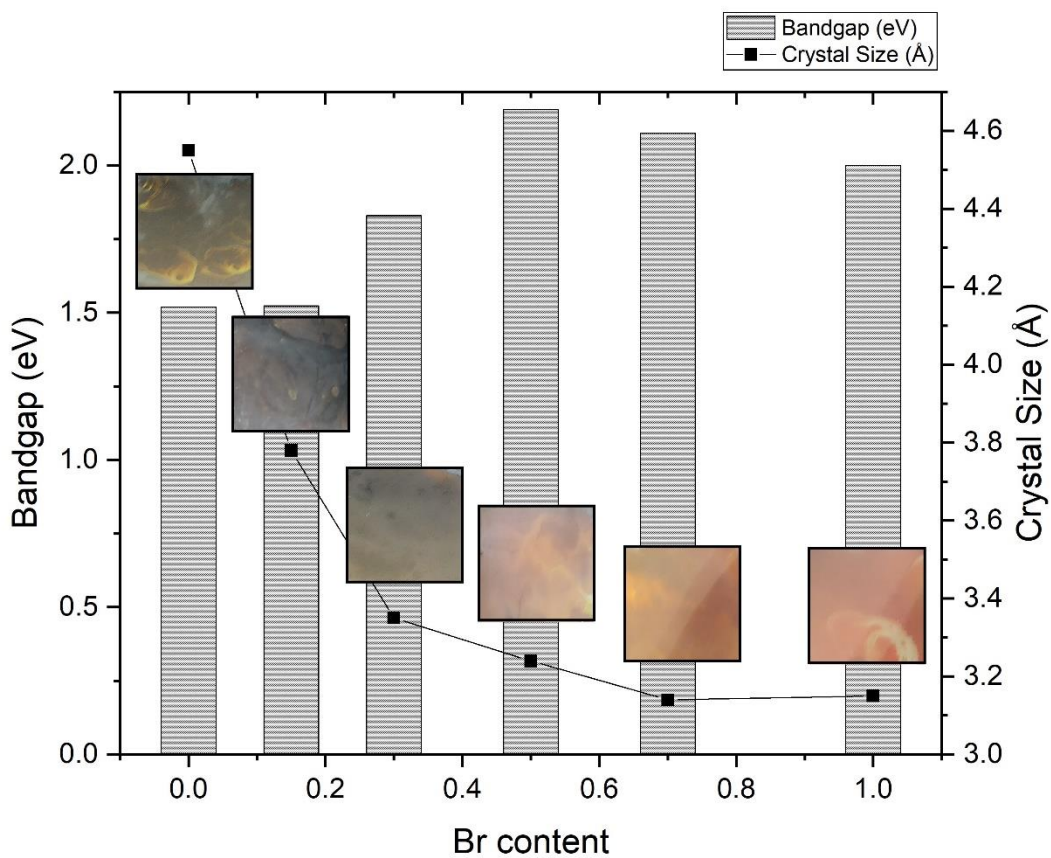
The crystal size of the different layers was calculated by analyzing the peaks from the XRD pattern. The peaks were fitted using a Gaussian distribution, and the full-width at half maximum (FWHM) was calculated. The size of the crystal was estimated using the Scherrer equation.

$$B(2\theta) = \frac{K\lambda}{L\cos\theta} \qquad [34]$$

Where B is the FWHM, K is the shape factor which and for simplicity assumed as 1, L is the crystallite size and ϑ is the peak angle in radians.

The crystallite size steadily decreases as the Br content is increased because of shrinking of the crystal lattice due to increasing concentration of the smaller Br^- ion. The bandgap increases with increasing Br but because of the likely mixed $CsPbBr_3$ phase it is much higher than what is reported in literature [15]. The insets show the color of the film also changed from black to red as the Br content was increased. This change in color indicates a phase shift as the composition becomes Br-rich [35].
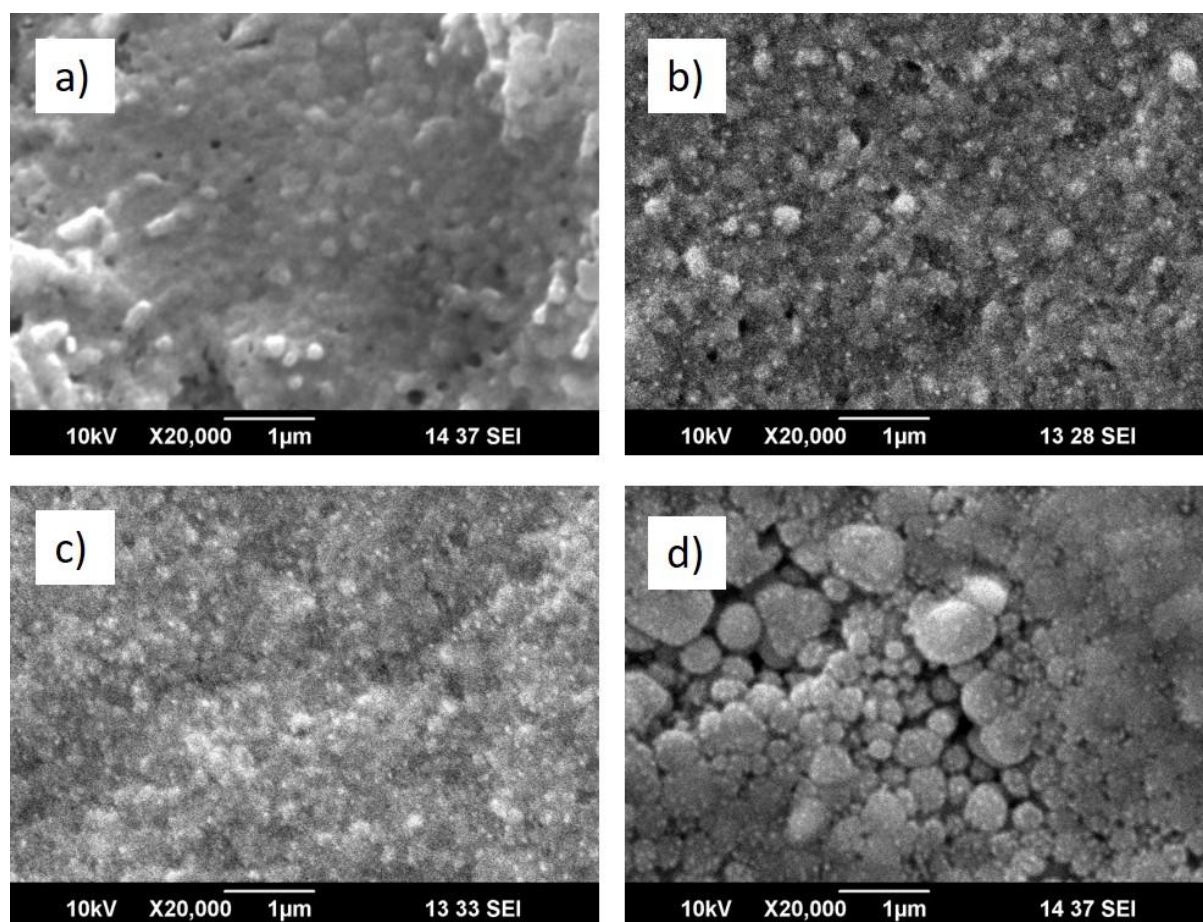
3.4 SEM and AFM Analysis

Figure 5 *SEM images for (a) $FA_{0.8}Cs_{0.2}PbI_{2.85}Br_{0.15}$ (b) $FA_{0.8}Cs_{0.2}PbI_{2.5}Br_{0.5}$ (c)$FA_{0.8}Cs_{0.2}PbI_{2.3}Br_{0.7}$ (d) $FA_{0.8}Cs_{0.2}PbI_2Br$ on glass substrate*

The SEM images in Fig. 5 are for four different film compositions. The Br-0.15 sample has smaller grains than the wide bandgap absorber layers reported in literature [14, 36] with a few voids visible in the film. As the concentration of Br is increased the Br-0.5 film shows more voids in between the grains which means there is uneven coverage. For Br-0.7, the grains become non-existent and the film has a very rough appearance. The coverage has somewhat improved but there is no crystalline order which was confirmed by the presence of multiple phases in our XRD pattern. For the Br-1 sample there are larger grains visible in the image. The average grain size was estimated to be 500 nm. These bubble-like grains have agglomerated together however, there are still some voids visible in the film.
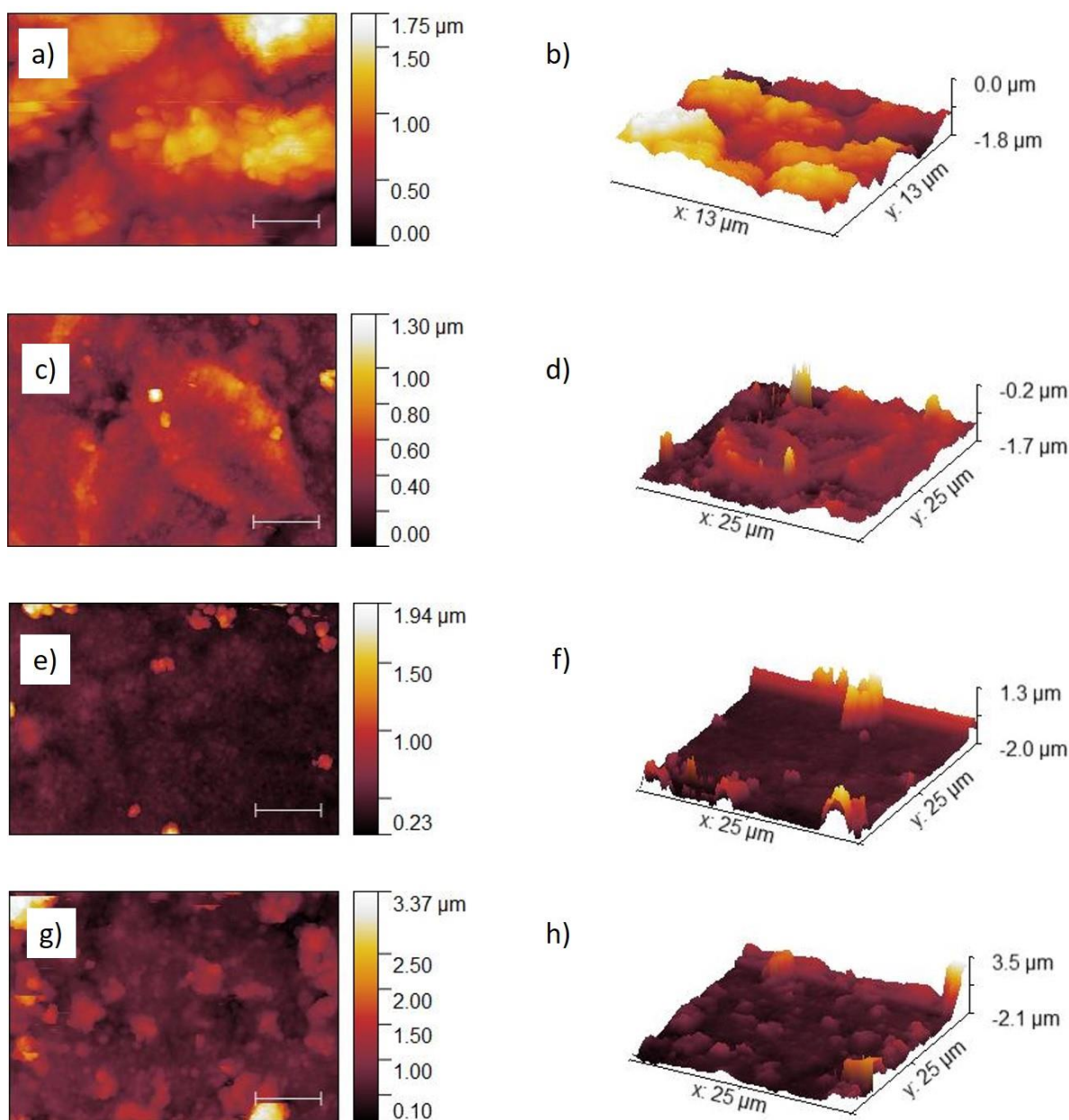
Figure 6 *AFM 2D images and 3D topography for (a, b) $FA_{0.8}Cs_{0.2}PbI_{2.85}Br_{0.15,}$ (c, d) $FA_{0.8}Cs_{0.2}PbI_{2.5}Br_{0.5}$, (e, f)$FA_{0.8}Cs_{0.2}PbI_{2.3}Br_{0.7,}$ (g, h) $FA_{0.8}Cs_{0.2}PbI_2Br$ on FTO substrate. The scale bar shown is 5 μm*

To investigate the roughness of the films and get an accurate idea of the grain size distribution of the film, the samples were characterized using AFM and the obtained images are reported in Figure 6. The Br-0.15 sample has an average grain size of 92.9 nm which was calculated by edge detection. For the Br-0.5 sample the value increased to 148.7 nm. The Br-0.7 perovskite layer saw a decrease in the grain size to 118 nm which can be explained by a decrease in the

crystallite size and is in agreement with the SEM results. When the Br content was increased to Br-1, the average grain size also increased to 348 nm.

The average roughness of the film for Br-0.15 was 68.7 nm and it increased to 110 nm for the Br-0.5 sample. Further increasing the Br content increased the roughness from 153 nm for Br-0.7 to 234 nm for Br-1 as it is evident by the non-homogenous topography. The AFM images show that the grain size increases by increasing the Br content of the film, and the roughness also varies in the same way. A rougher absorber layer helps trap more light and reduces reflectance losses [22], but due to the presence of voids, it may also affect device performance.

Conclusion

In conclusion, we studied the optical, morphological, and structural properties of mixed cation and mixed halide wide bandgap perovskite absorber layers fabricated through sequential deposition. The composition was tuned by keeping the FA and Cs ratio constant while varying the Br and I ratio. The samples exhibited a perovskite crystal phase and the crystallinity of the layer improved as the Br concentration was increased up to Br-0.3 as seen in the absorbance curves and XRD peaks. As the concentration was increased, a $CsPbBr_3$ perovskite phase emerged because the Br- ion is favored over the I- ion by the Pb atom. The absorption improves in the 300-500 nm range by increasing Br ratio which is encouraging for wide bandgap applications. The bandgap increased from 1.52 eV for the $FAPbI_3$ film to 1.83 eV for $FA_{0.8}Cs_{0.2}PbI_{2.7}Br_{0.3}$ however, further increase shifted the absorption onset drastically and the bandgap corresponds to that of $CsPbBr_3$. This confirms the presence of a $CsPbBr_3$ phase in the XRD pattern and implies that the I- ion is not incorporating itself into the perovskite crystal structure for samples with Br>0.3. The sequential deposition favors the lead bromide perovskite layer for a higher Br concentration because of the higher affinity for Pb towards Br. Increasing Br concentration increases the bandgap as predicted and improves crystallinity up to x = 0.3 for $FA_{0.8}Cs_{0.2}PbI_{3-x}Br_x$ in a two-step deposition procedure. Such wide bandgap

perovskite absorber layers are suitable as top cell for tandem solar cell applications and the bandgap can be further tuned according to the solar spectrum absorption window of the bottom cell.

References

1. Yin WJ, Yang JH, Kang J, Yan Y, Wei SH (2015) Halide perovskite materials for solar cells: A theoretical review. J Mater Chem A 3:8926–8942 . https://doi.org/10.1039/c4ta05033a

2. Hwang K, Jung Y-S, Heo Y-J, Scholes FH, Watkins SE, Subbiah J, Jones DJ, Kim D-Y, Vak D (2015) Toward Large Scale Roll-to-Roll Production of Fully Printed Perovskite Solar Cells. Adv Mater 27:1241–1247 . https://doi.org/10.1002/adma.201404598

3. Lin R, Xiao K, Qin Z, Han Q, Zhang C, Wei M, Saidaminov MI, Gao Y, Xu J, Xiao M, Li A, Zhu J, Sargent EH, Tan H (2019) Monolithic all-perovskite tandem solar cells with 24.8% efficiency exploiting comproportionation to suppress Sn(ii) oxidation in precursor ink. Nat Energy 4:864–873 . https://doi.org/10.1038/s41560-019-0466-3

4. Hou Y, Aydin E, De Bastiani M, Xiao C, Isikgor FH, Xue DJ, Chen B, Chen H, Bahrami B, Chowdhury AH, Johnston A, Baek SW, Huang Z, Wei M, Dong Y, Troughton J, Jalmood R, Mirabelli AJ, Allen TG, Van Kerschaver E, Saidaminov MI, Baran D, Qiao Q, Zhu K, De Wolf S, Sargent EH (2020) Efficient tandem solar cells with solution-processed perovskite on textured crystalline silicon. Science (80-) 367:1135–1140 . https://doi.org/10.1126/science.aay0262

5. Chen B, Yu ZJ, Manzoor S, Wang S, Weigand W, Yu Z, Yang G, Ni Z, Dai X, Holman ZC, Huang J (2020) Blade-Coated Perovskites on Textured Silicon for 26%-Efficient Monolithic Perovskite/Silicon Tandem Solar Cells. Joule 4:850–864 . https://doi.org/10.1016/j.joule.2020.01.008

6. Perovskite/silicon tandem solar cells approaching 30% efficiency in lab – pv magazine USA. https://pv-magazine-usa.com/2020/01/31/tandem-cells-approaching-30-efficiency/. Accessed 8 Jun 2020

7.   NREL Efficiency Chart

8.   Kieslich G, Sun S, Cheetham AK (2015) An extended Tolerance Factor approach for organic-inorganic perovskites. Chem Sci 6:3430–3433 . https://doi.org/10.1039/c5sc00961h

9.   Saliba M, Correa-Baena J-P, Grätzel M, Hagfeldt A, Abate A (2018) Perovskite Solar Cells: From the Atomic Level to Film Quality and Device Performance. Angew Chemie Int Ed 57:2554–2569 . https://doi.org/10.1002/anie.201703226

10. Hörantner MT, Leijtens T, Ziffer ME, Eperon GE, Christoforo MG, McGehee MD, Snaith HJ (2017) The Potential of Multijunction Perovskite Solar Cells. ACS Energy Lett 2:2506–2513 . https://doi.org/10.1021/acsenergylett.7b00647

11. Song Z, Chen C, Li C, Awni RA, Zhao D, Yan Y (2019) Wide-bandgap, low-bandgap, and tandem perovskite solar cells. Semicond Sci Technol 34:093001 . https://doi.org/10.1088/1361-6641/ab27f7

12. Kot M, Vorokhta M, Wang Z, Snaith HJ, Schmeißer D, Flege JI (2020) Thermal stability of CH3NH3PbIxCl3-x versus [HC(NH2)2]0.83Cs0.17PbI2.7Br0.3 perovskite films by X-ray photoelectron spectroscopy. Appl Surf Sci 513:145596 . https://doi.org/10.1016/j.apsusc.2020.145596

13. Szostak R, Marchezi E (2019) Sustainable Energy & Fuels Exploring the formation of formamidinium-based hybrid perovskites by antisolvent methods : in situ GIWAXS measurements during spin coating †. https://doi.org/10.1039/c9se00306a

14. Zhou Y, Jia YH, Fang HH, Loi MA, Xie FY, Gong L, Qin MC, Lu XH, Wong CP, Zhao N (2018) Composition-Tuned Wide Bandgap Perovskites: From Grain Engineering to Stability and Performance Improvement. Adv Funct Mater 28:1–8 . https://doi.org/10.1002/adfm.201803130

15. McMeekin DP, Snaith HJ, Sadoughi G, Rehman W, Eperon GE, Saliba M, Horantner

MT, Haghighirad A, Sakai N, Korte L, Rech B, Johnston MB, Herz LM, Snaith HJ (2016) A mixed-cation lead mixed-halide perovskite: The ideal absorber for tandem solar cells. Science (80-) 351:accepted . https://doi.org/10.1126/science.aad5845

16.   Lin Y, Chen B, Zhao F, Zheng X, Deng Y, Shao Y (2017) Matching Charge Extraction Contact for Wide-Bandgap Perovskite Solar Cells. 1700607:1–8 . https://doi.org/10.1002/adma.201700607

17.   Zheng L, Ma Y, Chu S, Wang S, Qu B, Xiao L, Chen Z, Gong Q, Wu Z, Hou X (2014) Improved light absorption and charge transport for perovskite solar cells with rough interfaces by sequential deposition. Nanoscale 6:8171–8176 . https://doi.org/10.1039/c4nr01141d

18.   Burschka J, Pellet N, Moon SJ, Humphry-Baker R, Gao P, Nazeeruddin MK, Grätzel M (2013) Sequential deposition as a route to high-performance perovskite-sensitized solar cells. Nature 499:316–319 . https://doi.org/10.1038/nature12340

19.   Zhao Y, Liu J, Lu X, Gao Y, You X, Xu X (2015) Improving the efficiency of perovskite solar cells through optimization of the CH 3 NH 3 PbI 3 film growth in solution process method. Appl Surf Sci 359:560–566 . https://doi.org/10.1016/j.apsusc.2015.10.132

20.   Xie Y, Shao F, Wang Y, Xu T, Wang D, Huang F (2015) Enhanced Performance of Perovskite $CH_3NH_3PbI_3$ Solar Cell by Using CH_3NH_3I as Additive in Sequential Deposition. ACS Appl Mater Interfaces 7:12937–12942 . https://doi.org/10.1021/acsami.5b02705

21.   Koh TM, Fu K, Fang Y, Chen S, Sum TC, Mathews N (2014) Formamidinium-Containing Metal-Halide: An Alternative Material for Near-IR Absorption Perovskite Solar Cells. https://doi.org/10.1021/jp411112k

22.   Kulkarni SA, Baikie T, Boix PP, Yantara N, Mathews N, Mhaisalkar S (2014) Band-gap tuning of lead halide perovskites using a sequential deposition process. J Mater

Chem A 2:9221–9225 . https://doi.org/10.1039/c4ta00435c

23. Koh TM, Krishnamoorthy T, Yantara N, Shi C, Leong WL, Boix PP, Grimsdale AC, Mhaisalkar SG, Mathews N (2015) Formamidinium tin-based perovskite with low Eg for photovoltaic applications. J Mater Chem A 3:14996–15000 . https://doi.org/10.1039/c5ta00190k

24. Ahmadian-yazdi MR, Zabihi F, Habibi M, Eslamian M (2016) Effects of Process Parameters on the Characteristics of Mixed-Halide Perovskite Solar Cells Fabricated by One-Step and Two-Step Sequential Coating. Nanoscale Res Lett. https://doi.org/10.1186/s11671-016-1601-8

25. Liang K, Mitzi DB, Prikas MT (1998) Synthesis and Characterization of Organic-Inorganic Perovskite Thin Films Prepared Using a Versatile Two-Step Dipping Technique. Chem Mater 10:403–411 . https://doi.org/10.1021/cm970568f

26. (2015) Artifacts in Absorption Measurements of Organometal Halide Perovskite Materials: What Are the Real Spectra? 3–7 . https://doi.org/10.1021/acs.jpclett.5b01406

27. Atourki L, Vega E, Marí B, Mollar M, Ait Ahsaine H, Bouabid K, Ihlal A (2016) Role of the chemical substitution on the structural and luminescence properties of the mixed halide perovskite thin MAPbI 3-X Br x (0 ≤ x ≤ 1) films. Appl Surf Sci 371:112–117 . https://doi.org/10.1016/j.apsusc.2016.02.207

28. Pengpad A, Ruankham P, Rattanachata A, Rattanasuporn S, Jenpiyapong W, Nakajima H, Choopun S, Amornkitbamrung V (2019) Surface composition of MAPb(I x Br 1−x) 3 (0 ≤ x ≤ 1) organic-inorganic mixed-halide perovskites. Appl Surf Sci 479:311–317 . https://doi.org/10.1016/j.apsusc.2019.02.105

29. Bi C, Shao Y, Yuan Y, Xiao Z, Wang C, Gao Y, Huang J (2014) Understanding the formation and evolution of interdiffusion grown organolead halide perovskite thin films by thermal annealing. J Mater Chem A 2:18508–18514 .

https://doi.org/10.1039/c4ta04007d

30. Eperon GE, Stranks SD, Menelaou C, Johnston MB, Herz LM, Snaith HJ (2014) Formamidinium lead trihalide: A broadly tunable perovskite for efficient planar heterojunction solar cells. Energy Environ Sci 7:982–988 . https://doi.org/10.1039/c3ee43822h

31. Ng CH, Ripolles TS, Hamada K, Teo SH, Lim HN, Bisquert J, Hayase S (2018) Tunable Open Circuit Voltage by Engineering Inorganic Cesium Lead Bromide/Iodide Perovskite Solar Cells. Sci Rep 8:1–9 . https://doi.org/10.1038/s41598-018-20228-0

32. Joon Yoon S, Kuno M, Kamat P V (2020) Shif t Happens. How Halide Ion Defects Influence Photoinduced Segregation in Mixed Halide Perovskites. 18:40 . https://doi.org/10.1021/acsenergylett.7b00357

33. Yoon SJ, Stamplecoskie KG, Kamat P V. (2016) How Lead Halide Complex Chemistry Dictates the Composition of Mixed Halide Perovskites. J Phys Chem Lett 7:1368–1373 . https://doi.org/10.1021/acs.jpclett.6b00433

34. Patterson AL (1939) The scherrer formula for X-ray particle size determination. Phys Rev 56:978–982 . https://doi.org/10.1103/PhysRev.56.978

35. Eperon GE, Stranks SD, Menelaou C, Johnston MB, Herz LM, Snaith HJ (2014) Formamidinium lead trihalide: A broadly tunable perovskite for efficient planar heterojunction solar cells. Energy Environ Sci 7:982–988 . https://doi.org/10.1039/c3ee43822h

36. Tan H, Che F, Wei M, Zhao Y, Saidaminov MI, Todorović P, Broberg D, Walters G, Tan F, Zhuang T, Sun B, Liang Z, Yuan H, Fron E, Kim J, Yang Z, Voznyy O, Asta M, Sargent EH (2018) Dipolar cations confer defect tolerance in wide-bandgap metal halide perovskites. Nat Commun 9: . https://doi.org/10.1038/s41467-018-05531-8